Inversion of Multi-Transient EM data from anisotropic media

M.Sc. Thesis

Dieter Werthmüller

Joint Master's in Applied Geophysics

TU Delft | ETH Zurich | RWTH Aachen

www.idealeague.org/geophysics

in collaboration with

Petroleum Geo-Services (PGS)

ElectroMagnetic Division PGS EM, Edinburgh

www.pgs.com

August 2009

Author

Dieter Werthmüller Dieter.Werthmuller@gmx.ch

Supervisors

Prof. B. A. Hobbs (PGS EM) Bruce.Hobbs@pgs.com

Prof. A. Ziolkowski (PGS EM) Anton.Ziolkowski@pgs.com

Dr. ir. E. Slob (TU Delft) E.C.Slob@tudelft.nl

A thesis submitted for the degree of

Master of Applied Earth Sciences	Delft University of Technology, The Netherlands
Master of Science in Applied Geophysics	Swiss Federal Institute of Technology Zurich, Switzerland
Master of Science in Applied Geophysics	Aachen University, Germany

Abstract

Forward modelling demonstrates that resistivity anisotropy has a huge effect on Multi-Transient ElectroMagnetic step and impulse responses. The earth is never isotropic – even a stack of isotropic layers behaves anisotropically – and there is a great need to account for resistivity anisotropy in order to delineate the true target depth and target transverse resistance in ElectroMagnetic surveying. I account for resistivity anisotropy by (a) deriving apparent anisotropy formulae and using them together with apparent resistivities for a fast iterative inversion scheme, and (b) by including anisotropy into a $1\mathcal{D}$ full waveform inversion scheme. Full anisotropic inversions result in much smoother models than isotropic inversions. Sharp resistivity boundaries result in anisotropy anomalies, as horizontal and vertical resistivities are not affected in the same way. Anisotropic inversion results yield a good indication of the present background anisotropy. Carrying out inversions with fixed anisotropies, e.g. determined in a free anisotropic inversion, can improve the result significantly compared with an isotropic inversion.

Acknowledgments

I am grateful to Bruce Hobbs, who introduced me to PGS EM in the first place by offering me an industrial placement in 2008. This thesis would not have taken place without his belief in me. I owe my deepest gratitude to my other supervisors, Anton Ziolkowski and Evert Slob, for their always professional and friendly assistance. It is a pleasure to thank those who made this thesis an exciting experience: My boss John Linfoot, who got never tired of explaining me details of the MTEM method over and over again, and all colleagues from PGS EM with their young and ethusiastic spirit. Keep on practicing tabletop football, I might be back some day! Gracias a mi cosita.

Contents

List of Figures

List of Tables

Notations and Conventions

The following is a list of symbols, conventions, definitions, special functions, and abbreviations which are consistently used throughout this thesis. Some entries are repeated and more extensively described in later chapters.

Symbols

Symbol	Description	SI Units
$\hat{E}_x$	amplitude of frequency response, normalised to a 1 Am source	Ωm^{-2}
$\dot{E}_x$	amplitude of impulse response, normalised to a 1 Am source	$\Omega m^{-2}s^{-1}$
E_x	amplitude of step response, normalised to a 1 Am source	Ωm^{-2}
G	earth impulse response	$\Omega m^{-2}s^{-1}$
μ_0	free space magnetic permeability; $\mu_0 = 4\pi \times 10^{-7}$ Hm^{-1}	Hm^{-1}
f	frequency	s^{-1}
d	layer thickness	m
V	measured voltage at receiver	V
ξ	misfit in empiric apparent anisotropy determination	–
χ	misfit in full waveform inversion	–
ζ	misfit in Zohdy method	–
N	noise	V
γ	normalisation parameter in frequency domain	–
τ	normalisation parameter in time domain	–
r	offset	m
Δx_r	receiver bipole length	m
μ	regularisation parameter in full waveform inversion	–
ρ	resistivity	Ωm
λ	resistivity anisotropy coefficient, or coefficient of anisotropy	–
I	source current	A
Δx_s	source bipole length	m
t	time	s
$\mathcal{R}$	transverse resistance	Ωm^2

Conventions

- **Anisotropy** refers to *Resistivity Anisotropy* unless explicitly otherwise stated.
- **1$\mathcal{D}$** one dimensional: all examples and results are for one dimensional models.
- $\boldsymbol{h}$**,** $\boldsymbol{m}$**,** $\boldsymbol{v}$ used as subscripts, stand for horizontal, mean and vertical.
- $\boldsymbol{\kappa}$ used as subscript, acts as wild-card for any of h, m, and v.
- $\boldsymbol{\mathcal{P}}_\kappa$ is used for constant resistivity, see Table 2.3.

Definitions

- (geometric) mean resistivity

$$\rho_m \;:=\; \sqrt{\rho_v \rho_h}$$

- resistivity anisotropy coefficient

$$\lambda \;:=\; \sqrt{\frac{\rho_v}{\rho_h}}$$

$\Rightarrow$ These definitions show the relationship between the different resistivity values

$$\lambda\rho_h \;=\; \rho_m \;=\; \frac{1}{\lambda}\rho_v$$

- transverse resistance

$$\mathcal{R} \;:=\; \lambda\rho_m d$$

- normalisation parameter in time domain

$$\tau_\kappa \;:=\; \sqrt{\frac{\mu_0 r^2}{\rho_\kappa t}}$$

- normalisation parameter in frequency domain

$$\gamma_\kappa \;:=\; \sqrt{\frac{\mu_0 r^2 s}{\rho_\kappa}} \qquad \text{with} \qquad s \;:=\; 2\pi \mathrm{i} f \quad \text{(Laplace parameter)}$$

Special Functions

Symbol		Description	Name
$\delta(x)$	$:=$	$0 \quad \text{if} \quad x \neq 0 \quad \text{and} \quad \int_{-\infty}^{\infty} \delta(x)dx = 1$	Dirac Delta Function
$\mathcal{H}(x)$	$:=$	$\begin{cases} 0 & \text{if} \quad x < 0 \\ 1/2 & \text{if} \quad x = 0 \\ 1 & \text{if} \quad x > 0 \end{cases}$	Step Function (Heaviside Function)
$\text{erf}(x)$	$:=$	$\frac{2}{\sqrt{\pi}} \int_0^x \exp\left(-t^2\right) dt$	Error Function

Abbreviations

Abbr.	Description
CSEM	Controlled Source ElectroMagnetic
DC	Direct Current
EM	ElectroMagnetic
IR	Impulse Response
MTEM	Multi-Transient ElectroMagnetic
NDIC	Normalised Depth of Investigation Characteristics
PRBS	Pseudo-Random Binary Sequence
SR	Step Response
TE	Transverse Electric
TI	Transverse Isotropy (also called polar or azimuthal anisotropy)
TM	Transverse Magnetic
VTI	Vertical Transverse Isotropy: TI with a vertical axis of symmetry

1

Introduction

1.1 Review

Electromagnetic methods have been widely used for academic and mining purposes since the early 20th century for the detection of conductors and resistors. They were extended to the marine environment around 1970, mainly for the academic interest of studying the solid earth (eg., Cheesman et al., 1987). It is just in this decade that electromagnetic offshore methods for hydrocarbon exploration were deployed and successfully commercialised, e.g., MTEM (today PGS EM), OHM, and EMGS. The latter two are working with a few harmonic frequencies and purely offshore, whereas the Multi-Transient ElectroMagnetic method from PGS has a transient signal and is a method that works both onshore and offshore. They all have in common that they use a controlled source (Controlled Source ElectroMagnetics). Edwards (2005) wrote an extensive overview of the principles, methodologies and commercial applications of CSEM. The interest in EM for hydrocarbon detection is that it can compensate for one of the major shortcomings of seismic surveys, the distinction between water and oil bearing rocks. Water and oil (but not gas) have similar acoustic properties, whereas their resistivities vary significantly.

The effects and the importance of anisotropy in controlled source electromagnetics has been well known (e.g., Edwards et al., 1984). The interest in anisotropy has intensified since the start of the hydrocarbon related EM companies. Lu and Xia (2007) showed that the effects of anisotropy on CSEM data are significant, and depend upon the transmitter-receiver geometry. Ramananjaona et al. (2008) inverted CSEM data to a $1\mathcal{D}$ resistivity model, and showed that the vertical resistivity detects a target very well, whereas the horizontal resistivity does not delineate a target. Jing et al. (2008) inverted $3\mathcal{D}$ data, indicating the need for $3\mathcal{D}$ data acquisition if one wants to delineate $3\mathcal{D}$ Vertical Transverse Isotropy (VTI). All these mentioned studies assumed VTI, but there is recently great interest in dealing with general TI (e.g., Løseth and Ursin, 2007; Greenhalgh et al., 2009).

Up to date, however, there have been no anisotropic inversions carried out for MTEM data.

1.2 My contribution

I show the effects of anisotropy on MTEM step and impulse responses on land and marine data for a uniform VTI half-space and a target in a uniform background. Important factors are the increase in non-uniqueness with the introduction of anisotropy, and the, in general, reduced depth of investigation for anisotropic data, which requires longer offsets to detect a target.

The late-time values of step responses allow calculation of apparent resistivities from MTEM data. I derive formulae to calculate in a similar manner apparent anisotropies from step responses, or from step and impulse responses. The Zohdy method enables the derivation of $1\mathcal{D}$ resistivity models from apparent resistivities, and I expand this method to anisotropic data and improve the method for isotropic data by using apparent anisotropies.

I include anisotropy into the $1\mathcal{D}$ full waveform inversion scheme `MTEM1D_INV` for both fixed anisotropic and free anisotropic inversions. The number of degrees of freedom is large for a full anisotropic inversion compared to an isotropic inversion, but I show that this gives an idea of

the present anisotropies and the background anisotropies. These background anisotropies can be put into a fixed anisotropy inversion to improve the inversion result.

1.3 Layout of this thesis

The essential background is provided in Chapter 2: A brief introduction to the MTEM method, an explanation of the standard models used in this thesis and their corresponding step and impulse responses, an explanation of Vertical Transverse Isotropy and some general remarks about anisotropy in electromagnetic measurements.

It is important to know the effects of anisotropy on MTEM data in order to interpret anisotropic inversion results. These effects are demonstrated in Chapter 3 for both uniform VTI half-spaces and targets embedded in a uniform background. The analytical solution for a uniform VTI half-space in the Laplace domain and in the time domain for step and impulse responses are given in the same chapter, together with information about the forward modellers used.

MTEM responses can be used to derive apparent anisotropy curves, similar to apparent resistivity curves. Two different methods are shown in Chapter 4. Apparent anisotropies are used in Chapter 5 to invert multi-offset data with an expanded Zohdy scheme. Isotropic, fixed anisotropic and free anisotropic full waveform inversion results are shown in Chapter 6. The final conclusions are drawn in Chapter 7.

The theoretical derivation for the anisotropic inversion is listed in Appendix A, and Appendix B shows examples of MTEM responses, decomposed into TE-mode and TM-mode. An example of a published expanded abstract is given in Appendix C, and some useful information for using the codes `MTEM1D_INV` and `ZOHDY_ANISO` can be found in Appendix D.

2

Background

MTEM method and anisotropy in EM sounding

The MTEM method has proven its capability in detecting hydrocarbon charged targets in the subsurface on- and offshore. Most research, data acquisition and data processing was done with the widely spread assumption of an isotropically resistive subsurface.

It is, however, well known in the EM community and in PGS EM that resistivity anisotropy is always present, and that it has a huge impact on electromagnetic measurements.

MTEM measurements are generally analysed as step or impulse response for land measurements. Only impulse responses are analysed for marine measurements, as the water layer filters out the interesting part of the airwave, the sudden step. These three responses have characteristic features, some of them sensitive to hydrocarbon targets.

Many research studies, mainly in the mining industry, have already been undertaken with interesting and important results. They can be simply applied to MTEM data or adjusted to suit the transient method.

2.1 MTEM method

The MTEM method is a relatively new technology for hydrocarbon detection, developed at Edinburgh University (e.g., Wright, 2003). It was later commercialised under MTEM Ltd., acquired by PGS in 2007. PGS combined it with the existing development of a towed EM system within PGS to PGS EM.

In the MTEM method current is injected into the ground between two electrodes (the source) and the resulting potential difference is measured between two further electrodes (the receiver). All four electrodes are collinear. The measured voltage at the receiver, $V(t)$, is given by

$$V(t) \;=\; \Delta x_s \Delta x_r I(t) * G(t) \;+\; N(t) \;, \tag{2.1}$$

where $I(t)$ is the source current, $G(t)$ the unknown impulse response of the earth (Greens function), $N(t)$ uncorrelated noise, t is time, and Δx_s and Δx_r the source and receiver bipole lengths. The distance between the midpoint of the source and the midpoint of the receiver is termed the offset r, and, in general, measurements for a range of different offsets are carried out. Transient current injection at the source may take the form of a step change in current, such as a reversal in polarity of a DC current, or a coded finite-length sequence such as a Pseudo-Random Binary Sequence (PRBS). For any form of the transient current injection, measurements are made of both the source current $I(t)$ and the receiver voltage $V(t)$. Deconvolution determines the earth's impulse response (IR) and integration of the impulse response yields the earth's step response (SR).

The main difference between MTEM and other CSEM methods is the source signal. CSEM uses a discrete harmonic frequency and multiples of it as a continuous signal, whereas MTEM uses a transient signal with a distinct beginning and end. This allows the measured signal to be deconvolved with the source current and obtain a much broader frequency spectrum. The transient input, the PRBS, has a much broader frequency range than standard CSEM, which usually only considers a fundamental frequency and a few odd harmonics.

MTEM step and impulse responses can be used to calculate common-offset sections, traveltime-to-resistivity mapping (using an apparent resistivity formula derived from the arrival time of the peak of the impulse), two-dimensional dipole-dipole DC resistivity inversions and full-waveform inversions. PGS published a comprehensive report about the role of electromagnetics in hydrocarbon exploration and the contribution of the newly acquired method in Long (2007). A case study showing the capabilities of MTEM is given by Ziolkowski et al. (2007).

2.2 Standard models and responses

Our standard models on land are shown in Figure 2.1a: A uniform isotropic half-space with resistivity $\rho = 20$ Ωm (blue model), and the same model as background including an isotropic, 25 m thick target at a depth of 500 m and resistivity $\rho = 500$ Ωm (red model). The corresponding step and impulse responses are shown in Figures 2.1b and 2.1c for an offset $r = 2$ km. The step responses show a sudden step immediately after switching the source on. This step is the

airwave, travelling with the speed of light through the upper half-space. The airwave is followed by the earth response, a response which tends to a constant value for $t \to \infty$. This late time value is equivalent to the DC value in dipole-dipole measurements. A high resistivity target leads to an increase in amplitude of the earth response. The impulse response is characterised by a delta peak at time $t = 0$ s, the airwave, followed by the earth impulse response. Land data can therefore be clearly separated into an airwave signal and an earth response. A high resistive target leads to higher amplitudes, similar to the step response, and to an earlier arrival of the peak of the impulse.

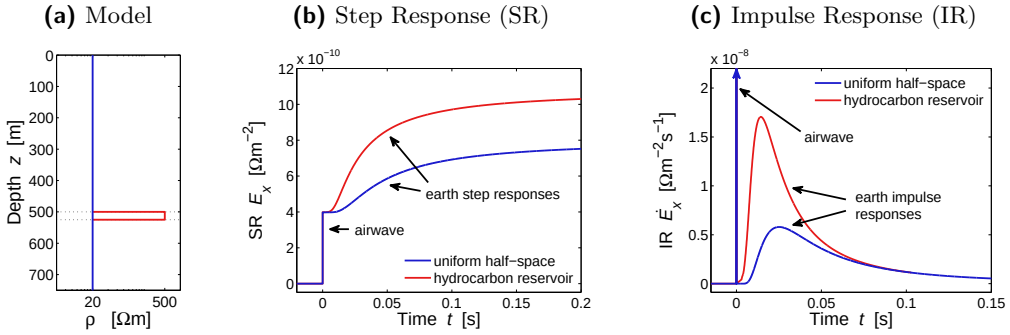

Figure 2.1: Earth's (b) step and (c) impulse responses for the standard land models shown in (a), calculated at an offset $r = 2$ km. A high resistivity target leads to an increase in amplitude and, for the IR, an earlier arrival of the peak.

The standard marine models are shown in Figure 2.2a: A uniform isotropic half-space with resistivity $\rho = 1$ Ωm below a 100 m water column with resistivity $\rho = 0.3$ Ωm (blue model), and the same model as background with an isotropic, 25 m thick target at 500 m depth and resistivity $\rho = 50$ Ωm (red model). The corresponding impulse responses are shown in Figure 2.2b. The airwave is attenuated by the water column, which causes an overlapping of the airwave and the earth response in the marine environment. This makes it difficult to clearly separate the airwave from the earth response. There are many methods seeking to remove the airwave from the signal. A simple method is given by Ziolkowski and Wright (2007): Calculating the signal $\dot{E}_{x,r_{\text{far}}}$ for a far offset r_{far}, scaling this response back to the desired offset r and subtracting it from the response $\dot{E}_{x,r}$,

$$\dot{E}^{\text{AR}}_{x,r} = \dot{E}_{x,r} - \left(\frac{r_{\text{far}}}{r}\right)^3 \dot{E}_{x,r_{\text{far}}} , \tag{2.2}$$

yields the airwave removed response $\dot{E}^{\text{AR}}_{x,r}$. The idea behind this approach is simple: The attenuation of the airwave due to the water layer is the same at every offset (from source to the surface and from the surface to the receiver). The airwave is not attenuated in the air, the decrease in amplitude is solely due to the geometrical spreading factor. The shape of the airwave is therefore constant, and can be scaled back. The airwave removed response is shown in Figure 2.2c, the far offset used is $r_{\text{far}} = 50$ km. It shows the same characteristics as the land impulse response: a high resistivity target results in a higher amplitude and an earlier arrival of the peak.

This airwave removal method cannot, however, remove the signal from the direct wave through the water column. Those effects can be significant for near offsets, but become negligible if the water depth is small compared with the offset. This can be seen in Figure 2.2c as the little peak for times $t < 0.5$ s.

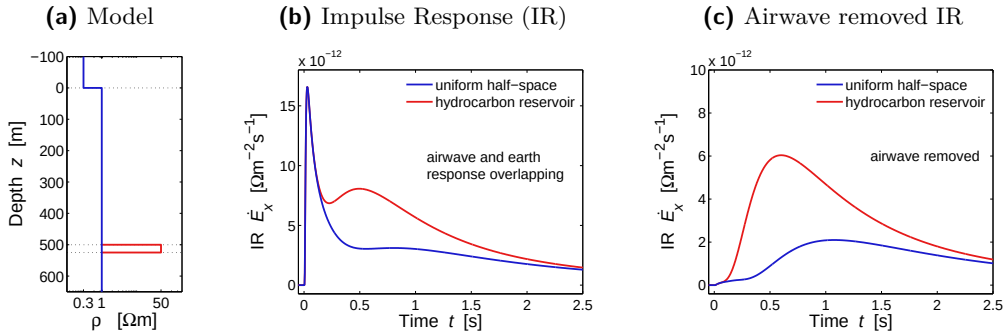

Figure 2.2: Earth's impulse responses (b) for the standard marine models shown in (a), calculated at an offset of $r = 3$ km. The responses are shown without the airwave in (c), which indicates that a high resistivity target leads to an increase in amplitude and an earlier arrival of the peak.

All modelled data show the inline electric-field step E_x [Ωm^{-2}] or impulse $\dot{E}_x$ [Ωm^{-2}s^{-1}] response at the surface for normalised source strength of 1 Am and receiver length of 1 m .

2.3 Resistivity Anisotropy and VTI

The simplest possible approximation for any physical property in a body is the uniform, isotropic assumption. Anisotropy is termed any variation of physical property depending on the direction in which it is measured. This volume might still be uniform, i.e. have the same anisotropic behaviour everywhere. Anisotropy occurs for most physical properties, e.g. in seismic wave propagation, heat conductance, cleavage properties. Observable anisotropic properties for the human eye are for instance the optical properties of some minerals, e.g. the birefringence of calcite. Resistivity anisotropy refers accordingly to different resistivity values in different directions.

The importance of resistivity anisotropy (simply termed *anisotropy* throughout this thesis) in electromagnetic measurements for prospecting and scientific purposes has been well known since the early 20th century, the beginning of electromagnetic sounding itself. Maillet (1947) summarised the most important insights into anisotropy. Bhattacharya and Patra (1968) treated anisotropy at length in their extensive book *Direct Current Geoelectric Sounding* twenty years later. And another twenty years later Negi and Saraf (1989) collated all knowledge together in their book *Anisotropy in Geoelectromagnetism*. All these publications were mainly considering traditional DC sounding, like Wenner or Schlumberger, or MagnetoTelluric measurements, with both a scientific or mining interest. Many of those relations, however, can be applied to transient measurements and hydrocarbon detection as well. A collection of basic relations

concerning anisotropy, which I consider as necessary for dealing with anisotropy, are given in the following. They are all, if not otherwise explicitly stated, from the above mentioned publications, which I highly recommend as introductory reading for anyone dealing with resistivity anisotropy.

The anisotropy under consideration is the so-called Vertical Transverse Isotropy (VTI), where the resistivity in any horizontal direction, ρ_h, can be different from the vertical resistivity ρ_v, see Figure 2.3a. They define the coefficient of anisotropy λ,

$$\lambda := \sqrt{\frac{\rho_v}{\rho_h}} , \tag{2.3}$$

and the (geometric) mean resistivity ρ_m,

$$\rho_m := \sqrt{\rho_v \rho_h} . \tag{2.4}$$

Equations 2.3 and 2.4 define the relationship between the different resistivity values,

$$\lambda\rho_h = \rho_m = \frac{1}{\lambda}\rho_v . \tag{2.5}$$

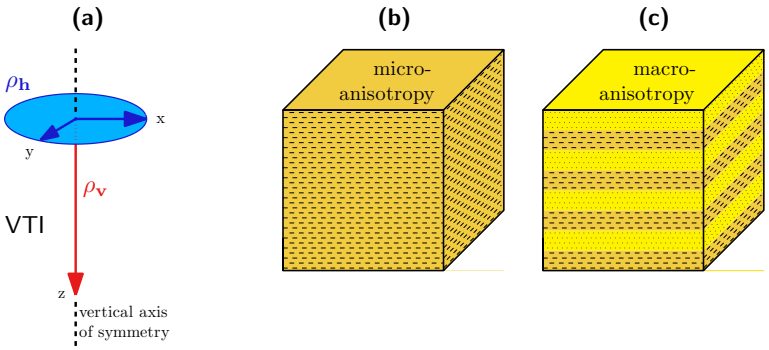

Figure 2.3: Explanatory illustrations for (a) Vertical Transverse Isotropy (VTI) and the difference between (b) micro- and (c) macro-anisotropy; total anisotropy being the superimposition of both.

Micro-anisotropy describes anisotropy within a homogeneous formation, e.g. flat and parallel aligned minerals as mica in clay sediments, see Figure 2.3b. *Macro-anisotropy* occurs from varying resistivities in formations below resolution thickness, e.g. shale-sandstone sequences, as shown in Figure 2.3c. The formations causing macro-anisotropy may contain micro-anisotropy themselves; the superimposed micro- and macro-anisotropy is termed *total anisotropy*.

The geological assumption for VTI is that of horizontal layered sediments, where horizontal resistivities are usually smaller than vertical resistivities, i.e. $\lambda > 1$. The range of anisotropy values in the literature is broad. They generally range from 1, e.g. for clean and uniform sandstone, to 2 - 3, e.g. for limestones or limey shales, up to 7 and higher for interbedded anhydrite and shales. I assume a typical range for a hydrocarbon host environment to have an anisotropy between 1 and 3. This assumption obviously fails in regions with dipping or

Table 2.1: The three different $\mathcal{P}_\kappa$ for changing anisotropy coefficients.

$\boldsymbol{\mathcal{P}_h}$	:	ρ_h	=	const.	$\Longrightarrow$	ρ_v	$\Uparrow$	and	ρ_m	$\Uparrow$	with	λ	$\Uparrow$
$\boldsymbol{\mathcal{P}_m}$	:	ρ_m	=	const.	$\Longrightarrow$	ρ_h	$\Downarrow$	and	ρ_v	$\Uparrow$	with	λ	$\Uparrow$
$\boldsymbol{\mathcal{P}_v}$	:	ρ_v	=	const.	$\Longrightarrow$	ρ_h	$\Downarrow$	and	ρ_m	$\Downarrow$	with	λ	$\Uparrow$

highly deformed structures, strong tectonic stresses, or non-horizontal fracturing. In extreme situations, such as strong vertical fractures, the anisotropy can become lower than 1.

Any two out of the four parameters ρ_h, ρ_m, ρ_v, and λ define a system in terms of VTI resistivities. Increasing or decreasing anisotropy itself can therefore have different meanings. The most useful way to analyse anisotropy is to increase or decrease the anisotropy coefficient by keeping the horizontal, mean, or vertical resistivity constant. These three scenarios are denoted by $\mathcal{P}_\kappa$, where κ stands for the resistivity which is kept constant. Their relative effects are listed in Table 2.3.

Another important concept is the transverse resistance. A layer with resistivity ρ and thickness d behaves like a layer of twice the thickness but half the resistivity, i.e. it gives the same response as long as the product of thickness and resistivity remains constant. This ambiguity increases with the introduction of anisotropy. The transverse resistance for VTI is given by

$$\mathcal{R} = \lambda \rho_m d \,, \tag{2.6}$$

where ρ_m can be replaced according to Equation 2.5.

A value of great importance in electromagnetic sounding is the depth of investigation, which was conceptually introduced by Evjen (1938). Bhattacharya and Sen (1981) extended the expression of Normalised Depth of Investigation Characteristics (NDIC) to the general TI case; both assuming $\mathcal{P}_m$. Following their derivation, the NDIC for VTI MTEM responses is given by

$$\begin{aligned}\mathrm{NDIC}_{\mathrm{MTEM}} = \frac{4\lambda^2 z}{\frac{1}{\mathcal{A}_+^-} - \frac{1}{\mathcal{A}_-^-} - \frac{1}{\mathcal{A}_+^+} + \frac{1}{\mathcal{A}_-^+}}\,\mathrm{d}z \Bigg\{ &\frac{1}{\left[\mathcal{A}_+^{-\,2} + 4\lambda^2 z^2\right]^{3/2}} \\ &- \frac{1}{\left[\mathcal{A}_-^{-\,2} + 4\lambda^2 z^2\right]^{3/2}} - \frac{1}{\left[\mathcal{A}_+^{+\,2} + 4\lambda^2 z^2\right]^{3/2}} + \frac{1}{\left[\mathcal{A}_-^{+\,2} + 4\lambda^2 z^2\right]^{3/2}} \Bigg\} \,,\end{aligned} \tag{2.7}$$

where

$$\begin{aligned}\mathcal{A}_+^- &= r - \frac{\Delta x_s}{2} + \frac{\Delta x_r}{2} \,, & \mathcal{A}_+^+ &= r + \frac{\Delta x_s}{2} + \frac{\Delta x_r}{2} \,, \\ \mathcal{A}_-^+ &= r + \frac{\Delta x_s}{2} - \frac{\Delta x_r}{2} \,, & \mathcal{A}_-^- &= r - \frac{\Delta x_s}{2} - \frac{\Delta x_r}{2} \,.\end{aligned}$$

In this definition r is the offset from source midpoint to receiver midpoint, Δx_s the source length and Δx_r the receiver length.

Figure 2.4b shows the NDIC for a typical MTEM layout with source and receiver width $\Delta x_s = \Delta x_r = 100$ m, offset $r = 2$ km and the VTI assumption for a range of anisotropies. It shows clearly that the depth of investigation rapidly decreases with increasing anisotropy for $\mathcal{P}_m$. This has to be considered for both determining the acquisition layout and determining initial starting models for an inversion scheme. The figure also illustrates what is meant by NDIC: the area below every curve is equal to unity, and the amplitudes indicate how much a given depth contributes to the total response. Some values even become negative, although with very small amplitudes; they indicate negative contribution to the total response.

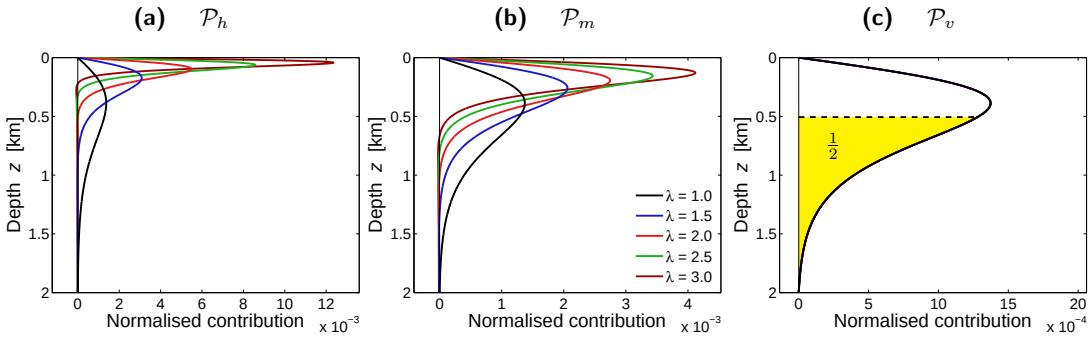

Figure 2.4: Normal Depth of Investigation Characteristics for (a) $\mathcal{P}_h$, (b) $\mathcal{P}_m$, and (c) $\mathcal{P}_v$. The depth of investigation is rapidly decreasing with increasing anisotropy for $\mathcal{P}_h$ and $\mathcal{P}_m$. Anisotropy does not affect the depth of investigation, if the vertical resistivity is kept constant. Note that the isotropic, black curve is the same in every plot.

Bhattacharya and Sen (1981) showed that one achieves the solution for VTI by taking the isotropic solution for NDIC and replacing the isotropic resistivity ρ by the mean resistivity ρ_m, z by λz and $\mathrm{d}z$ by $\lambda \mathrm{d}z$, i.e. in the same way as one achieves the VTI transverse resistance from the isotropic transverse resistance in Equation 2.6. The anisotropy coefficient λ has to be replaced by λ^2 and by 1 to achieve the NDIC for $\mathcal{P}_h$ and $\mathcal{P}_v$ respectively; the corresponding curves are shown in Figures 2.4a and 2.4c. They show, not surprisingly, that the depth of investigation is faster decreasing for $\mathcal{P}_h$, and that it is not affected at all for $\mathcal{P}_v$ (all curves lie behind the black line). Edwards (1977) defined the *effective depth* as the depth, at which one-half of the total response originates from above, and one-half from below. The effective depth is indicated for $\mathcal{P}_v$ by the black dashed line.

One has to keep in mind that this analysis is done for DC resistivity. It is no indication for the transient part, e.g. the effective depth for the peak of the impulse response. It can, however, be regarded as an upper limit, as the DC resistivity is the part of the response which penetrates the deepest.

Summary

I explained the MTEM method and illustrated the considered standard models with their corresponding responses for both land step and impulse as well as marine impulse responses. I explained the concepts of VTI, micro-, macro- and total anisotropy. Much research has already been carried out for anisotropic EM responses, the most important concepts are described. It has always to be kept in mind what is meant by increasing anisotropy. I introduced the terminology of $\mathcal{P}_\kappa$, standing for constant resistivity ρ_κ with increasing anisotropy, for easy referencing. The ambiguity of anisotropic EM measurements is denoted by the transverse resistance. The penetration to depth is decreasing with increasing anisotropy for $\mathcal{P}_h$ and $\mathcal{P}_m$, but is unaffected for $\mathcal{P}_v$.

3

Forward modelling

Effects of anisotropy on MTEM data

Varying anisotropy coefficients have a huge impact on MTEM responses. These impacts are different for constant horizontal, mean, or vertical resistivity, the three cases defined in Chapter 2 ($\mathcal{P}_\kappa$). It is crucial to understand the effects of varying resistivity anisotropy before determining anisotropy coefficients through any inversion scheme.

MTEM responses for a uniform VTI half-space can be calculated analytically, and numerical forward modellers are used for any model of higher complexity. Step and impulse responses have characteristic elements, which can be related to horizontal, mean, or vertical resistivity. The airwave, for example, is affected only by the horizontal resistivity of a thin top layer. Anisotropy increases the non-uniqueness of MTEM responses, and the penetration depth generally decreases with increasing anisotropy.

3.1 Analytical solutions

The analytical solution for the electric field in a uniform VTI half-space generated by an electric current source below the surface of a non-conductive half-space (air) is given by Slob (E. Slob, personal communication, 2009) in the Laplace domain. This solution is for a source at $x^s = 0$, $y^s = 0$ and any depth $z^s \geq 0$ (positive z direction pointing downwards) and a receiver at any point in the subsurface ($x^r,\ y^r,\ z^r \geq 0$). Simplifying this solution for $1\mathcal{D}$ MTEM responses with source and receiver inline and at the surface ($x^s = 0,\ y^s = 0,\ z^s = 0;\ y^r = 0,\ z^r = 0$), and denoting x^r by the offset r, yields the analytical Laplace domain solution for $1\mathcal{D}$ uniform VTI half-space MTEM response, given by Equation 3.1:

Laplace Domain

$$\hat{E}_x(\rho_h, \lambda, r, s) \;=\; \frac{\rho_h}{2\pi r^3}\left[1 \;-\; \exp\left(-\gamma_h\right) \;+\; (2\lambda \;+\; \gamma_h)\exp\left(-\frac{\gamma_h}{\lambda}\right)\right] \tag{3.1}$$

For notations refer to Notations and Conventions on page 13; $\gamma_h = \sqrt{\mu_0 s r^2/\rho_h}$, $s \;=\; 2\pi \mathrm{i} f$. Note that the solution is given in terms of horizontal resistivity and anisotropy coefficient. It may, however, be rewritten in any combination of at least two parameters out of ρ_h, ρ_m, ρ_v, and λ. Our forward modeller and inversion codes work with ρ_h and λ, this explains my choice of ρ_h and λ. The Laplace domain solution can be transformed to time domain for a step response or an impulse response, as given by Equations 3.2 and 3.3:

Time Domain: Step Response $\mathcal{H}(\mathbf{t})$

$$E_x(\rho_h, \lambda, r, t) \;=\; \frac{\rho_h}{2\pi r^3}\left[2\lambda \;+\; \mathrm{erf}\left(\frac{\tau_h}{2}\right) \;-\; 2\lambda\,\mathrm{erf}\left(\frac{\tau_h}{2\lambda}\right) \;+\; \frac{\tau_h}{\sqrt{\pi}}\exp\left(-\frac{\tau_h^2}{4\lambda^2}\right)\right] \tag{3.2}$$

Time Domain: Impulse Response $\delta(\mathbf{t})$

$$\dot{E}_x(\rho_h, \lambda, r, t) \;=\; \frac{\rho_h}{2\pi r^3}\left[\delta(t) \;+\; \frac{\tau_h}{2t\sqrt{\pi}}\left\{-\exp\left(-\frac{\tau_h^2}{4}\right) \;+\; \left(\frac{\tau_h^2}{2\lambda^2} \;+\; 1\right)\exp\left(-\frac{\tau_h^2}{4\lambda^2}\right)\right\}\right] \tag{3.3}$$

where $\tau_h = \sqrt{\mu_0 r^2/(\rho_h t)}$.

Note that Equations 3.2 and 3.3 reduce to the isotropic solution for $\lambda = 1$,

$$E_x(\rho, r, t) \;=\; \frac{\rho}{2\pi r^3}\left[2 \;-\; 2\,\mathrm{erf}\left(\frac{\tau}{2}\right) \;+\; \frac{\tau}{\sqrt{\pi}}\exp\left(-\frac{\tau^2}{4}\right)\right]\ , \qquad \text{(Weir (1980), 6.13)}$$

and

$$\dot{E}_x(\rho, r, t) \;=\; \frac{\rho}{2\pi r^3}\left[\delta(t) \;+\; \frac{\tau^3}{4t\sqrt{\pi}}\exp\left(-\frac{\tau^2}{4}\right)\right]\ , \qquad \text{(Wilson (1997), 5.38)}$$

as derived by the indicated authors.

3.2 Forward modeller

We made use of two different forward modellers: `MTEM1D` calculates the response in the time domain using the Gaver-Stehfest algorithm (written by R. N. Edwards, University of Toronto). `INTEM1D` calculates the response in the frequency domain using a logarithmic Fast Fourier Transformation (impulse response) and a convolution method (step response) for the transformation to time domain (written by the Consortium for Electromagnetic Modeling and Inversion, CEMI). Both can handle VTI, when provided with the horizontal resistivity ρ_h and the anisotropy coefficient λ as input.

Having two different forward modellers has the advantage of testing them one against each other. It allows us additionally to model and invert with different codes which reduces systematic errors.

Many forward modellers handling VTI seem to work with horizontal resistivity and the anisotropy coefficient. Often publications therefore discuss $\mathcal{P}_h$ solely, the case of constant horizontal resistivity. This one-sided approach should be avoided, as it describes not all features of anisotropy. $\mathcal{P}_h$ means increasing mean resistivities with increasing anisotropies. Effects caused by higher resistivities might therefore untruly be declared as anisotropy effects.

3.3 Uniform half-space

The simplest model to study any response is a uniform isotropic half-space. Our standard models and their MTEM responses are explained and shown in Section 2.1. On land it is a uniform half-space with resistivity $\rho = 20$ Ωm. In the marine environment it consists of a uniform half-space with resistivity $\rho = 1$ Ωm below a 100 m water column with resistivity $\rho = 0.3$ Ωm (receiver placed on the seabed). To study the effects of anisotropy we vary the anisotropy coefficients λ for all cases of $\mathcal{P}_\kappa$, transforming the uniform isotropic half-space into a uniform VTI half-space. Note that the resistivity property of water (and air) is always isotropic.

Step response on land

The effects of anisotropy on an MTEM land step response are shown in Figure 3.1 for the three different cases $\mathcal{P}_\kappa$. Figure 3.1a shows increasing amplitudes with increasing anisotropy coefficients for $\mathcal{P}_h$, whereas Figure 3.1c shows decreasing amplitudes for $\mathcal{P}_v$. This is because mean resistivities ρ_m increase with increasing anisotropy coefficients for $\mathcal{P}_h$ and decrease for $\mathcal{P}_v$, see the definitions for the three cases $\mathcal{P}_\kappa$ in Table 2.3.

The step responses have the same amplitudes of the initial step disregarding the value of the anisotropy coefficients for $\mathcal{P}_h$, shown in Figure 3.1a. Figure 3.1b shows that they approach in a similar manner the same late-time values for $\mathcal{P}_m$. These two observations can also be derived

from the analytical solutions. Taking the limits for $t \to 0$ and $t \to \infty$ of Equation 3.2 yields values for the step early-time E_x^0 and late-time E_x^∞ amplitudes,

$$\lim_{t\to 0} E_x(\rho_h, \lambda, r, t) \;=\; E_x^0 \;=\; \frac{\rho_h}{2\pi r^3} \tag{3.4}$$

and

$$\lim_{t\to \infty} E_x(\rho_h, \lambda, r, t) \;=\; E_x^\infty \;=\; \frac{\rho_h \lambda}{\pi r^3}\,. \tag{3.5}$$

It can be seen from Equations 3.4 and 3.5 that the early-time amplitude is only dependent on the horizontal resistivity ρ_h, and the late-time on the mean resistivity $\rho_m = \rho_h\lambda$. These relationships are used for an apparent anisotropy determination in Section 4.2.

This also makes it clear that there is no uniform isotropic half-space resulting in the same step response as a uniform VTI half-space, because it is not possible to change λ while keeping both ρ_h and ρ_m constant. See Appendix B for more information about the importance of ρ_h and ρ_v throughout the response.

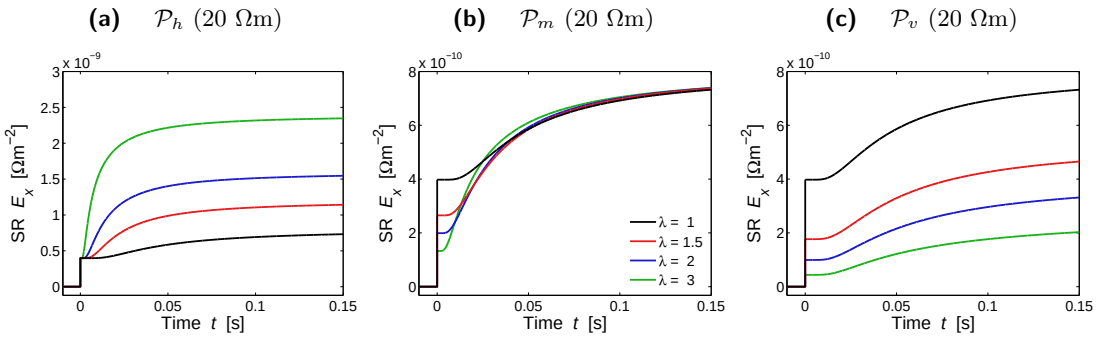

Figure 3.1: Effects of anisotropy on a land step response for a uniform VTI half-space; $r = 2$ km. Note that the isotropic response (black) is identical for all $\mathcal{P}_\kappa$. Time axis is kept constant for better comparison.

Impulse response on land

The same standard model as for a land step response is shown in Figure 3.2 for a land impulse response. The amplitudes increase for $\mathcal{P}_h$ and decrease for $\mathcal{P}_v$ for increasing anisotropy coefficients, similar to the step responses. There is, however, no equivalent relationship for the early-time and late-time amplitudes as there is for the step response. The airwave is a peak with infinite amplitude at $t = 0$, and the earth response starts after the airwave with zero amplitude and goes back towards zero for the late-time values.

Figure 3.2c shows a characteristic feature of the impulse response: The arrival time of the peak is mainly dependent on the vertical resistivity ρ_v. Higher vertical resistivities cause an earlier arrival of the peak, as can be seen in the cases $\mathcal{P}_h$ and $\mathcal{P}_m$. This also shows that, similar to the step response, there is no uniform isotropic half-space resulting in the same impulse response

as a uniform VTI half-space. This property is extensively discussed in Section 4.3, and used for another apparent anisotropy determination.

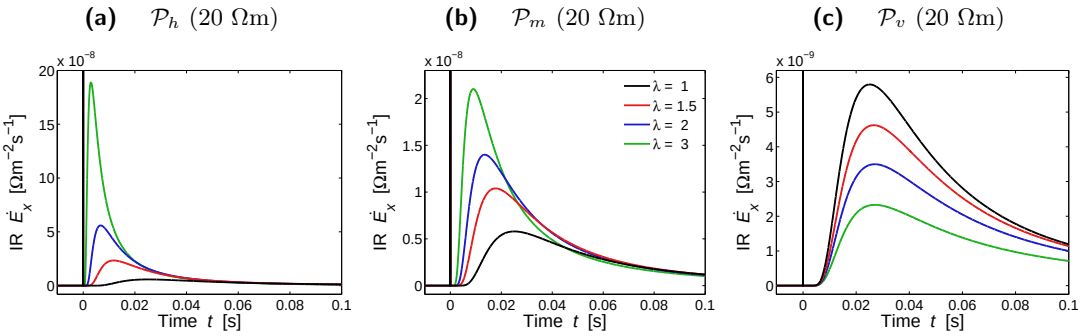

Figure 3.2: Effects of anisotropy on a land impulse response for a uniform VTI half-space; $r = 2$ km. Note that the isotropic response (black) is identical for all $\mathcal{P}_\kappa$. Time axis is kept constant for better comparison.

Impulse response for marine

The effects of anisotropy on a marine impulse response are shown in Figure 3.3 for the three different cases of $\mathcal{P}_\kappa$. The responses have similar characteristics to land impulse responses, namely increasing amplitudes of the earth response with increasing anisotropy for $\mathcal{P}_h$ (3.3a) and $\mathcal{P}_m$ (3.3b), and decreasing amplitudes for $\mathcal{P}_v$ (3.3c). The responses are dominated by the airwave, which overlaps the earth response in marine responses. Figure 3.3a indicates that the responses at early times depend only on the horizontal resistivity. This cannot solely be attributed to the airwave, as in the land step response, because the marine response is a combination of contributions from the earth, the water layer and the air at all times.

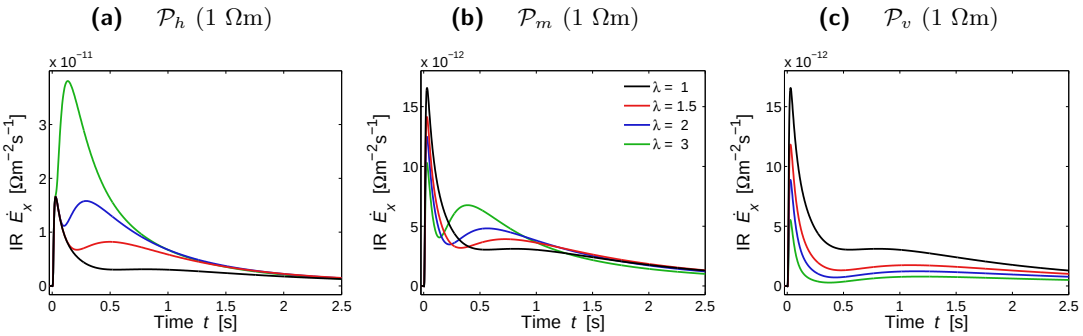

Figure 3.3: Effects of anisotropy on a marine impulse response for a uniform VTI half-space; $r = 3$ km. Note that the isotropic response (black) is identical for all $\mathcal{P}_\kappa$. Time axis is kept constant for better comparison.

When the airwave is removed from the marine responses, as shown in Section 2.1, the marine

responses resemble almost the land impulse responses in Figure 3.2 (almost because there is also a contribution from the water layer). The model and the offset are different, and so are the time and amplitude axes, but the shape of the responses and the effects of anisotropy are comparable. The infinity spike at $t = 0$ is missing, which is the airwave for the land case. An early-time signal occurs due to the water layer. There are direct and multiple waves travelling through the water column, causing also secondary airwaves.

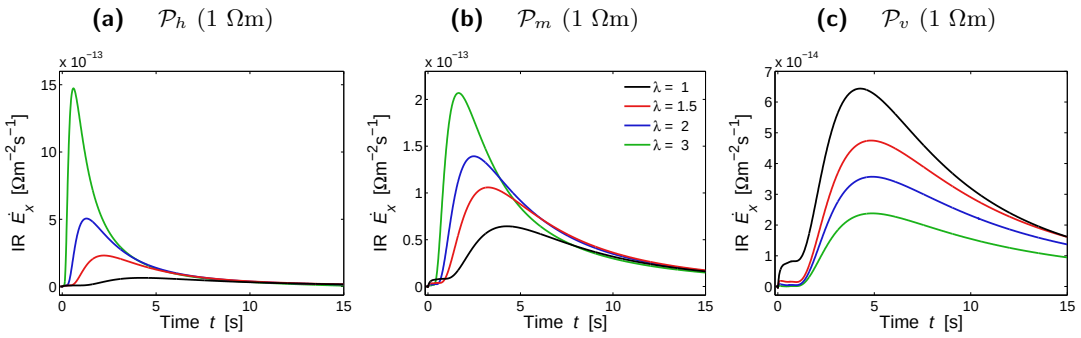

Figure 3.4: Effects of anisotropy on a marine impulse response with removed airwave for a uniform VTI half-space; $r = 6$ km. Note that the isotropic response (black) is identical for all $\mathcal{P}_\kappa$. Time axis is kept constant for better comparison.

The responses in Figures 3.3 and 3.4 are modelled at different offsets, 3 km and 6 km respectively. The contributions from the water layer are significant at an offset of 3 km and would dominate the airwave-removed impulse response. At an offset of 6 km, on the other hand, the airwave amplitude is significantly bigger than the amplitude of the earth response, so that the changes due to anisotropy would not clearly appear by showing the whole response. Two different offsets are therefore chosen in order to show as clearly as possible the effects of anisotropy.

3.4 Target embedded in uniform background

The next simple model after a uniform VTI half-space is a target in a uniform background, both target and background being VTI volumes with either the same anisotropy coefficients or different. The standard target model on land is a 25 m thick, isotropic layer with resistivity $\rho_t = 500$ Ωm at a depth of $z = 500$ m in an isotropic background with resistivity $\rho_b = 20$ Ωm. The depth models and their corresponding MTEM responses for land and marine standard target models are shown and explained in Section 2.1.

Three questions are answered within this Section:

1. How much information about the subsurface is contained in the airwave?
2. What are the relative influences of background and target anisotropy?
3. How does anisotropy affect the non-uniqueness in MTEM responses?

Question 1 is answered using the example of a land step response, Question 2 with a land impulse response and Question 3 with land step and impulse responses. This choice was made with respect to the response that shows it the best. The answers apply, however, to all responses.

Airwave

We have seen that the airwave has a huge impact on MTEM responses, and is only dependent on the horizontal resistivity, as shown in Figure 3.1. This suggests the possibility of determining the anisotropy coefficients of the subsurface, assuming that the airwave is influenced by the same volume as the earth response. Figure 3.5 shows that this is not the case.

Figure 3.5a shows the depth-model for the three different responses at an offset of $r = 2$ km in Figure 3.5b. The standard response (black) is a uniform isotropic half-space with resistivity $\rho = 20$ Ωm. The lower response (green) has an isotropic, 50 m thick top-layer with the same resistivity, and below a uniform isotropic half-space with resistivity $\rho = 10$ Ωm. The higher response (red) has an isotropic, 100 m thick top-layer with the same resistivity, and below a uniform isotropic half-space with resistivity $\rho = 30$ Ωm. The initial step amplitude, the airwave, is the same for all three responses. But they diverge immediately after the initial step due to the shallow more conductive and more resistive subsurfaces.

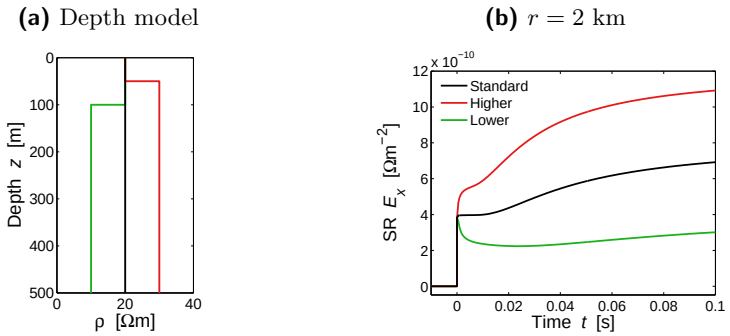

Figure 3.5: The airwave is only dependent on a thin top surface layer. Half-space for $\rho = 20$ Ωm (black), lower resistivity in 50 m (green) and higher resistivity in 100 m (red) depth have the same initial step. $\lambda = 1$ for all responses.

The exact thickness of the top layer which influences the airwave is presumed to be a function of resistivity and offset. It is supposedly related to the travel-time of the airwave from source to receiver, and the depth which the electromagnetic wave can penetrate in this time and interact with the airwave (diffusion depth). It is, however, only a thin top layer of a few tens of metres.

This has a huge impact for the land case, where the shallow subsurface in the real $3\mathcal{D}$ world is highly inhomogeneous, the so-called *weathering layer*. This causes highly varying airwaves and therefore step amplitudes, which cannot be modelled with a $1\mathcal{D}$ forward modeller.

Non-uniqueness in VTI MTEM responses

Targets, deep enough not to affect the airwave, with the same transverse resistance $\mathcal{R} = \lambda\rho_m d$ generate very similar EM responses, as explained Section 2.3. EM inversion routines are for this reason always constrained, e.g., the Occam inversion (Constable et al., 1987), which seeks to find the smoothest model.

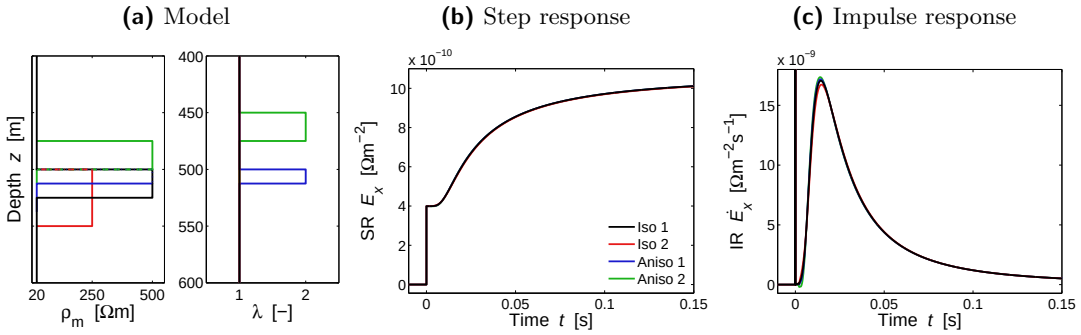

Figure 3.6: Non-uniqueness in VTI MTEM responses I: The responses for the depth models in (a) are shown for a step in (b), and for an impulse in (c). There are only small differences, not distinguishable for an inversion.

Figure 3.6 shows some example of non-uniqueness. The black line is our isotropic standard model. The red line shows an isotropic model with double the target thickness, but half the target resistivity. The blue model is an anisotropic target with $\lambda = 2$, the same mean resistivity $\rho_m = 500$ Ωm but half the target thickness. They all give (almost) the same step and impulse responses.

Another non-uniqueness is shown in the green model: the target is identical with the standard target, but 25 m shallower. Above the target is a layer with the same mean resistivity as the whole overburden and the same thickness as the target, but with an anisotropy of $\lambda = 2$. This target also generates the same step and impulse responses. This means, theoretically, that anisotropy can shift a target to any depth in an inversion scheme.

By having a closer look at the responses one would detect small differences, specifically at intermediate times. These differences are, however, not big enough to affect any inversion scheme.

Figure 3.7 shows the influence of ρ_κ on the transverse resistance, $\mathcal{R} = \lambda^2\rho_h d = \lambda\rho_m d = \rho_v d$. All models have an isotropic background with $\rho = 20$ Ωm, and a target thickness of $d = 25$ m. The black and the blue models have the same horizontal target resistivity, the black and the red models have the same vertical target resistivity. The step and impulse responses for the three models in Figures 3.7b and 3.7c show that a target with $\mathcal{P}_v$ and constant thickness yields the same response for any anisotropy. This is the reason why inversion schemes struggle to reveal appropriate horizontal resistivities, as shown in Chapter 6.

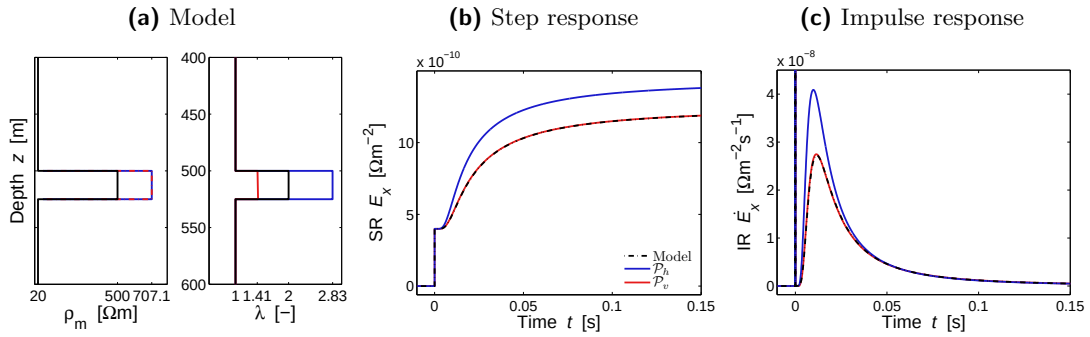

Figure 3.7: Non-uniqueness in VTI MTEM responses II: The responses for the depth models in (a) are shown for a step in (b), and for an impulse in (c). The responses for $\mathcal{P}_v$ are identical.

Background versus target anisotropy

The penetration depth decreases with increasing anisotropy coefficient, as described in Section 2.3. Figures 3.8 and 3.9 show the importance of background and target resistivities. The black response is a uniform VTI half-space without a target. The other responses have a standard target with varying anisotropy for $\mathcal{P}_m$ as annotated. The responses detect the target and distinguish different target anisotropies at an offset of $r = 1.5$ km for an isotropic background. The responses do not reach the target any more for a background anisotropy of $\lambda_b = 3$.

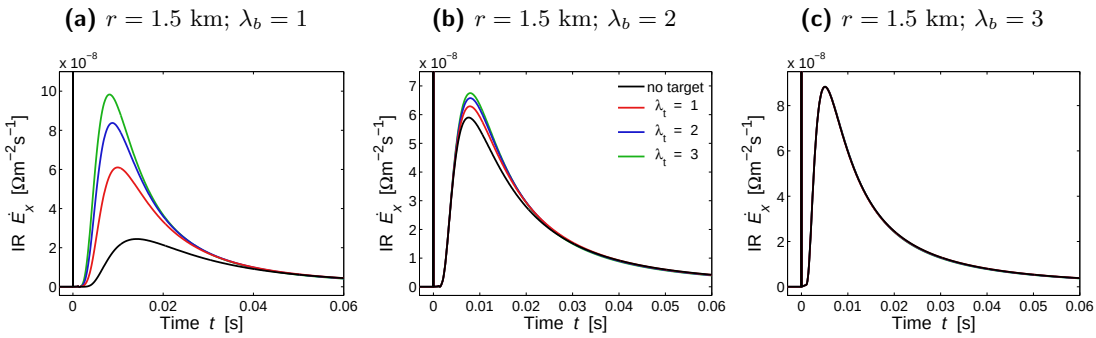

Figure 3.8: The penetration depth is decreasing with increasing anisotropy. For background anisotropy $\lambda_b = 3$ the targets at 500 m depth are not detected any more at an offset $r = 1.5$ km. All responses are for $\mathcal{P}_m$, with background resistivity $\rho_m = 20$ Ωm and target resistivity $\rho_m = 500$ Ωm.

The responses for the model with background anisotropy $\lambda = 3$ start to detect the target and delineate target anisotropy with increasing offset. Different target anisotropies are always distinguishable. If, on the other hand, the background anisotropy is not known, the target might never be detected, or be put at a wrong depth.

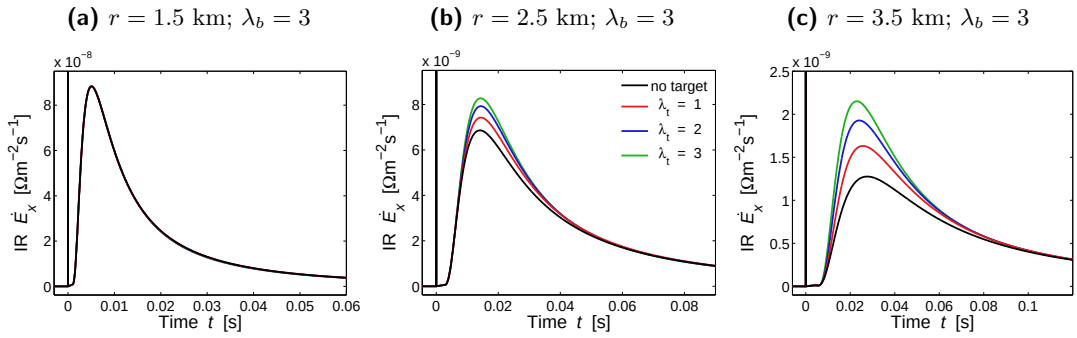

Figure 3.9: Longer offsets are required for VTI to delineate targets. Different target anisotropies are always distinguishable, if the target is detected. All responses are for $\mathcal{P}_m$, with background resistivity $\rho_m = 20$ Ωm and target resistivity $\rho_m = 500$ Ωm.

Summary

I listed the analytical solution for a uniform VTI half-space in Laplace domain and in time domain for step and impulse responses. The effects of anisotropy on MTEM responses are huge and differ for different $\mathcal{P}_\kappa$. Early-time E_x^0 and late-time E_x^∞ amplitudes of uniform VTI half-spaces depend only on the horizontal ρ_h and mean ρ_m resistivity respectively. Arrival time of the peak of the impulse response depends mainly on the vertical resistivity ρ_v. The airwave removed marine response shows the same characteristics for $\mathcal{P}_\kappa$ as the land impulse response. The airwave is only dependent on the horizontal resistivity, and only affected by a thin top layer. Anisotropy increases the non-uniqueness of MTEM responses. Larger offsets are needed with increasing anisotropy to penetrate the same depth for $\mathcal{P}_h$ and $\mathcal{P}_m$.

4

Apparent anisotropy

Determining anisotropies for equivalent half-spaces

Apparent resistivity curves are often used for elementary interpretation of DC resistivity measurements, or in addition to more sophisticated interpretation methods. The idea is to calculate for any measurement the uniform half-space resistivity which would generate the measured response. These calculated apparent resistivities are then plotted as a function of offset.

Apparent anisotropy curves can be calculated in a similar manner. Edwards et al. (1984) proposed an apparent anisotropy formula in the frequency domain. I derive two time domain apparent anisotropy formulae for MTEM data. These formulae provide an indication of the present anisotropy values with simple calculations before any inversion scheme is applied.

4.1 Characteristics of MTEM responses

Standard MTEM responses and the effects of anisotropy are shown in Chapters 2 and 3. Figure 4.1 repeats and defines characteristic properties of step and impulse responses, which are used in the later described apparent anisotropy methods.

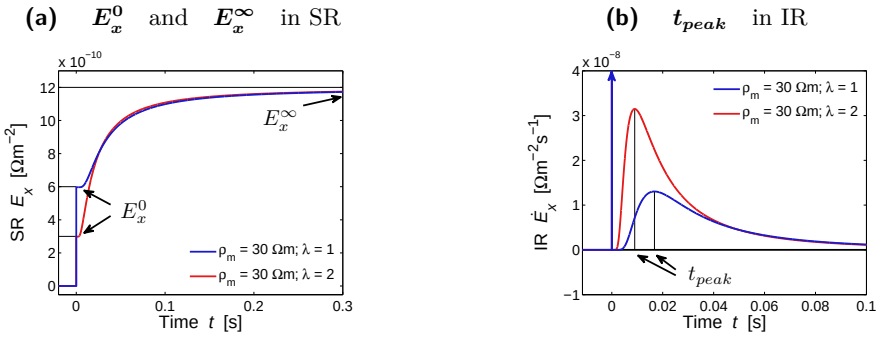

Figure 4.1: Characteristics of MTEM responses: early-time amplitudes (E_x^0) and late-time or DC amplitudes (E_x^∞) in step responses; arrival times of peak (t_{peak}) in impulse responses. The two curves show the responses for uniform VTI half-spaces with mean resistivity $\rho_m = 30$ Ωm, and anisotropy of $\lambda = 1$ (blue) and $\lambda = 2$ (red).

The Airwave arrives almost instantaneously in the step response, with amplitude denoted E_x^0. The step response approximates a constant value for $t \to \infty$, with amplitude denoted E_x^∞. The arrival time of the peak in the impulse response is termed t_{peak}. The two different curves show two uniform VTI half-spaces with mean resistivity $\rho_m = 30$ Ωm, therefore $\mathcal{P}_m$. The blue model has anisotropy $\lambda = 1$, the red model has $\lambda = 2$.

4.2 Airwave method

The following method is the subject of US Patent Application No. 12/381,690 (Hobbs and Werthmüller, 2009), titled *Method for determining resistivity anisotropy from earth electromagnetic responses*. The airwave method uses the limits $t \to 0$ and $t \to \infty$ for the analytical, anisotropic solution of the step response, as derived in Equations 3.4 and 3.5,

$$E_x^0 = \frac{\rho_h}{2\pi r^3} \quad \text{and} \quad E_x^\infty = \frac{\rho_h \lambda}{\pi r^3} \,. \qquad \text{(Equations 3.4, 3.5)}$$

These relations can be rearranged to give the anisotropy coefficient for a uniform VTI half-space in terms of the early-time and late-time amplitudes. Applying this anisotropy coefficient to a non-uniform half-space yields an apparent anisotropy,

$$\lambda_{a,a} = \frac{E_x^\infty}{2E_x^0} \,. \qquad (4.1)$$

Taking into account that the late-time value is only dependent on the mean resistivity $\rho_m = \rho_h \lambda$ and equivalent to the DC value, yields the apparent resistivity ρ_a if applied to a non-uniform half-space,

$$\rho_a \;=\; \pi r^3 E_x^{\infty} \tag{4.2}$$

The apparent anisotropy curve is obtained by calculating the defined apparent anisotropy value for a range of offsets and plotting them as a function of offset. Figure 4.2 shows some explanatory examples, which illustrate the possibilities and limitations of this method. The models are defined in Figure 4.2a in terms of ρ_m and λ. The depth-range is a close-up of the target area; the values stay constant above 400 m and below 600 m. Every line not visible lies behind the black line. The apparent anisotropy and apparent resistivity curves for these models are shown in Figure 4.2b and 4.2c.

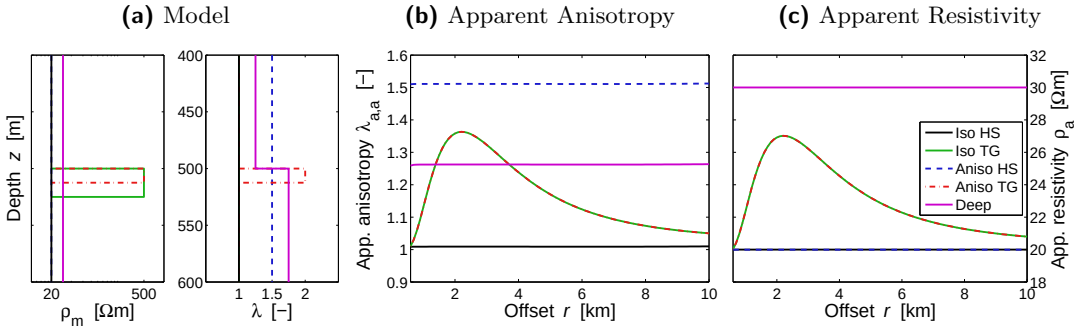

Figure 4.2: Apparent anisotropy curves using the airwave method. Close-up of the interesting section of the depth structure is given in (a); all invisible lines are behind the black line. The corresponding apparent anisotropy $\lambda_{a,a}$ and apparent resistivity ρ_a curves are given in (b) and (c); the green and the red are identical in both, the blue and the black in the apparent resistivity. See text for detailed explanation.

Uniform isotropic (solid black) and anisotropic (dashed blue) half-spaces yield, not surprisingly, the true anisotropy coefficient and the true resistivity for all offsets. An isotropic target (solid green) appears anisotropic on the surface, with varying apparent anisotropy coefficients. The problem of non-uniqueness, as shown in Section 3.4, is not solved with this method, as seen in the exact same apparent anisotropy curve for the equivalent anisotropic target (dash dotted red).

The limitations are demonstrated with the purple model, and by comparing the apparent anisotropy curve with the apparent resistivity curve. The early-time values are only affected by a relatively thin top layer. A half-space with uniform mean resistivity, but changing anisotropy coefficient at 500 m depth is not resolved by this method. The comparison of the apparent anisotropy and the apparent resistivity shows that, unless the top layer is anisotropic as in the blue and the purple model, the apparent anisotropy curve is a scaled apparent resistivity curve, scaled by the horizontal resistivity of the top layer.

Conclusion

The airwave method is a very easy method. The formula $E_x^{\infty}/(2E_x^0)$ allows us to draw even by hand within minutes an apparent anisotropy curve for a range of offsets. The information content is, however, very limited and does not provide significantly more information than the apparent resistivity curve.

Nevertheless, this method provides a good estimate of the present anisotropy coefficient for the near surface. Calculating the apparent anisotropy for small offsets allows us to define the anisotropy relatively accurately for the top layer, the overburden. These values can constrain background models for more sophisticated inversions and presumably significantly improve them.

4.3 Peak method

The following method is the subject of US Patent Application No. 12/460,183 (Hobbs and Werthmüller, 2009), titled *Method for determining resistivity anisotropy from earth electromagnetic transient step response and electromagnetic transient peak impulse response.* The peak method uses the result shown in Figure 3.2c: the arrival time of the peak is mainly dependent on the vertical resistivity. The analytical solution for a uniform VTI half-space impulse response is given in Equation 3.3. The partial derivative with respect to time is given by

$$\ddot{E}_x = \frac{\rho_h \tau_h}{16 r^3 \sqrt{\pi^3 t^3}} \left[\left(3 - \frac{\tau_h^2}{2} \right) \exp\left(-\frac{\tau_h^2}{4} \right) + \left(\frac{\tau_h^4}{4\lambda^4} - \frac{2\tau_h^2}{\lambda^2} - 3 \right) \exp\left(-\frac{\tau_h^2}{4\lambda^2} \right) \right] , \quad (4.3)$$

where the airwave is neglected. Setting this derivative to zero yields a formula with respect to the arrival time of the peak t_p,

$$\frac{12\lambda^4 + 8\tau_h^2\lambda^2 - \tau_h^4}{2\lambda^4 (6 - \tau_h^2)} - \exp\left(-\frac{\tau_h^2}{4} \left\{ 1 - \frac{1}{\lambda^2} \right\} \right) = 0 , \quad (4.4)$$

where $\tau_h = \sqrt{\frac{\mu_0 r^2}{\rho_h t_p}}$.

Applying Equation 4.4 to a non-uniform VTI half-space yields an apparent anisotropy coefficient $\lambda_{a,p}$,

$$\frac{12\lambda_{a,p}^6 + 8\tau_m^2\lambda_{a,p}^3 - \tau_m^4}{2\lambda_{a,p}^5 (6\lambda_{a,p} - \tau_m^2)} - \exp\left(-\frac{\tau_m^2}{4\lambda_{a,p}} \left\{ 1 - \frac{1}{\lambda_{a,p}^2} \right\} \right) = 0 , \quad (4.5)$$

where we assume that the mean resistivity is known from the late-time value of the step response, as given in Equation 4.2, and τ_m is given by

$$\tau_m = \sqrt{\frac{\mu_0 r^2}{\rho_m t_p}} = \sqrt{\frac{\mu_0}{\pi r E_x^{\infty} t_p}} . \quad (4.6)$$

This equation can be solved numerically to derive the exact (numerical) apparent anisotropy coefficient.

To get an, although empirical, analytical solution we assume an isotropic half-space, which allows us to solve Equation 4.3 for t_p,

$$t_p \;=\; \frac{\mu_0 r^2}{10\rho}\;. \tag{4.7}$$

We have seen that the arrival time is mainly dependent on the vertical resistivity, but not solely. We split ρ by a linear relation into $\alpha\rho_v \;+\; (1-\alpha)\rho_h$. Figure 4.3 shows the error ξ, a weighted root mean square function, as a function of the fraction α, where ξ is calculated by

$$\xi(\alpha) \;=\; \left[\frac{1}{MNO}\sum_{i=0}^{M}\sum_{j=1}^{N}\sum_{k=1}^{O}\left(\frac{\alpha\rho_{hk}\lambda_j \;+\; (1\;-\;\alpha)\rho_{hk} \;-\; \rho^{calc}(\rho_{hk},\lambda_j,r_i)}{\rho^{calc}(\rho_{hk},\lambda_j,r_i)}\right)^2\right]^{1/2}\;. \tag{4.8}$$

The empirical solution is derived by calculating a broad range of models, as given in Figure 4.3. The best misfit is achieved for $\alpha = 0.9$ with $\xi = 1.08$ %.

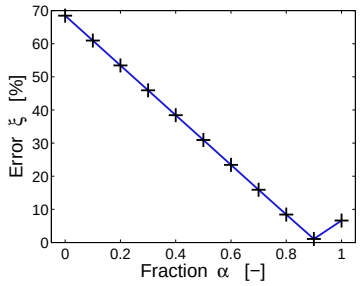

$$\begin{aligned}\rho_h &= 1, 2, \ldots, 99, 100\ \Omega\text{m}\\ \lambda &= 1.0, 1.1, \ldots, 2.9, 3.0\\ r &= 0.1, 0.2, \ldots, 9.9, 10.0\ \text{km}\\ \alpha &= 0.0, 0.1, \ldots, 0.9, 1.0\end{aligned}$$

Figure 4.3: Empirical approximation for peak method: The error ξ plotted as a function of α, for all combinations of ρ_h, λ, and r as indicated. The best misfit is achieved for $\alpha = 0.9$ with $\xi = 1.08$ %.

We use this result to derive an approximate apparent anisotropy $\lambda'_{a,p}$, assuming again that the mean resistivity is given from the late-time step response. By replacing ρ with $0.9\rho_v + 0.1\rho_h$, substituting ρ_h by $\rho_m/\lambda'_{a,p}$, and ρ_v by $\rho_m\lambda'_{a,p}$ in Equation 4.7 results in the quadratic equation

$$9{\lambda'_{a,p}}^2 \;-\; \tau_m^2\lambda'_{a,p} \;+\; 1 \;=\; 0\;. \tag{4.9}$$

The larger root is the appropriate solution, as we assume the vertical resistivity to be greater than the horizontal resistivity, i.e. $\lambda > 1$. This defines the empirical, analytical apparent anisotropy $\lambda'_{a,p}$,

$$\lambda'_{a,p} \;=\; \frac{\tau_m^2 \;+\; \sqrt{\tau_m^4 \;-\; 36}}{18} \;=\; \frac{\mu_0}{18\pi r E_x^{\infty} t_p}\left(1 \;+\; \sqrt{1 \;-\; \frac{36\pi^2 r^2 {E_x^{\infty}}^2 t_p^2}{\mu_0^2}}\right)\;. \tag{4.10}$$

Apparent anisotropy curves resulting from the peak method are shown in Figure 4.4 for the same models as for the airwave method before. The depth structures are given in Figure 4.4a, the values remain constant above 400 m and below 600 m. The thick coloured lines are the results for the numerical solution $\lambda_{a,p}$, the thin black lines with the same pattern below are the corresponding result with the empirical solution $\lambda'_{a,p}$.

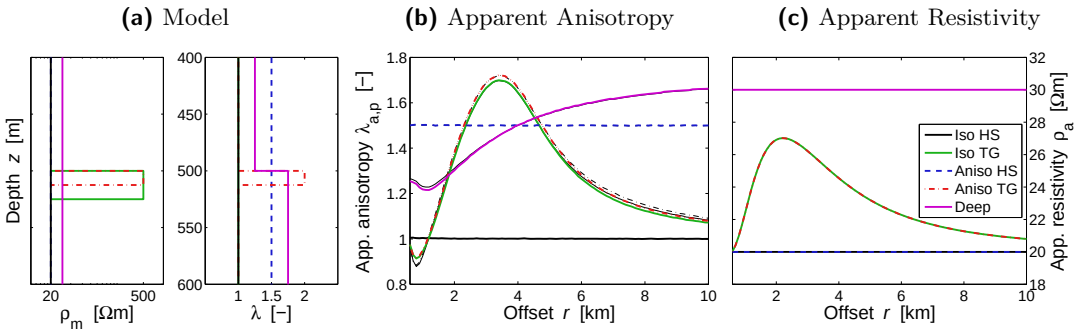

Figure 4.4: Apparent anisotropy curves using the peak method. Close-up of the interesting section of the depth structure is given in (a); all invisible lines are behind the black line. The corresponding apparent anisotropy $\lambda_{a,p}$ and apparent resistivity ρ_a curves are given in (b) and (c). The bold coloured lines are calculated with the exact numerical method, the corresponding thin black lines below with the empirical approximation. See text for detailed explanation.

The method reveals the true anisotropy coefficients for uniform isotropic (solid black) and anisotropic VTI half-spaces. An isotropic target model (solid green) appears anisotropic on the surface, and slightly different from the equivalent anisotropic target model (dash dotted red). This indicates that the apparent anisotropy curve can help to lessen the non-uniqueness of EM measurements.

The differences from the airwave method can be seen in the target models, and the model with changing anisotropy in 500 m depth. The peak method is able to distinguish between changing anisotropies in depth for $\mathcal{P}_m$, unlike the airwave method (solid purple). Comparing the apparent anisotropy and the apparent resistivity curves shows that they contain different information.

There is a possible explanation for the dip before the increase by the green, red and purple models: The late-time value travelled deeper than the peak value and can see a target earlier. This effect causes lower apparent anisotropies.

Conclusion

The peak method is superior to the airwave method for one main reason: the information used (E_x^{∞}) and (t_{peak}) which travelled through similar volumes, and the apparent anisotropy values yield therefore good estimates for this volume.

This advantage comes with a cost: both impulse and step response are needed, and the calculation is not purely analytical anymore, or empirical.

In theory, it is possible to extract apparent anisotropy values from the peak value only, analysing the arrival time and the amplitude of the peak. Many solutions are very close to each other, and it was not possible to get a stable routine, even with synthetic data.

Summary

I have shown two methods (airwave and peak) to determine apparent anisotropy values, using the early-time E_x^0 and late-time E_x^∞ values of the step response and the arrival time of the peak t_{peak} from the impulse response. Both methods have advantages and disadvantages. The airwave method allows quick interpretation of anisotropy values from step responses. It allows us to determine accurate near-surface anisotropy values, but the usage for deeper parts is limited. The peak method is able to detect deep anisotropies even for $\mathcal{P}_m$, and gives valuable information additional to the apparent resistivity curves.

5

Anisotropic Zohdy

Zohdy method including apparent anisotropy

Zohdy (1989) proposed "a new method for the automatic interpretation of Schlumberger and Wenner sounding curves". The method generates in a fast iterative manner a $1\mathcal{D}$ resistivity model from apparent resistivities for a range of offsets in two steps: first determining layer thicknesses, and second determining layer resistivities.

Apparent anisotropies, as described in Chapter 4, yield information for every offset in addition to the apparent resistivities used by the Zohdy method. I show a method to (a) expand the Zohdy method to anisotropic data and (b) improve the Zohdy method for isotropic data by making use of apparent anisotropies.

5.1 Zohdy method

The Zohdy method requires DC resistivity measurements at a number of offsets from which apparent resistivities are calculated. In the MTEM method these apparent resistivities are calculated from the step responses at every offset by applying Equation 4.2. The assumptions for the initial model are that the number of layers is equal to the number of offsets, the depths of the layers are equal to half the corresponding offsets, and the resistivities are equal to the apparent resistivities. Starting from this initial model, the Zohdy method determines in two steps the layer thicknesses and layer anisotropies.

The first step determines the layer thicknesses

1.1. Assume the initial model is the true model.

1.2. Calculate the step responses for this model at every offset and calculate the corresponding apparent resistivities.

1.3. Calculate the misfit ζ between the measured and the calculated apparent resistivities,

$$\zeta = \sqrt{\frac{1}{N}\sum_{j=1}^{N}\left(\frac{\rho_j^{a,o} - \rho_j^{a,c}}{\rho_j^{a,o}}\right)^2}, \tag{5.1}$$

where N is the number of layers (or offsets), a indicates apparent, and o, c stand for observed and calculated.

1.4. Decrease all layer thicknesses by 10 % (or another small amount).

1.5. Repeat Steps 1.2 and 1.3 and compute a new misfit ζ.

1.6. Compare the new misfit ζ with the old one. If it is smaller it means that the apparent resistivity curves are more in phase, and the model depths are closer to the unknown true depths.

1.7. Repeat Steps 1.4, 1.2, 1.3, and 1.6 until the misfit increases, which indicates that the layers are compressed too much.

The thickness determination is shown in Figure 5.1b: The black circles are the apparent resistivities from our "measurements" (in this case calculated from our synthetic standard model, Section 2.2) at a number of offsets. The thin dashed blue line through the black dots illustrates the initial depth-resistivity model gained from the measurements. Calculating the apparent resistivities for this model yields the thick blue curve (Steps 1.2 and 1.3). The final model after the thickness determination is given by the purple line. The corresponding depth-resistivity models are shown in Figure 5.1a, note that the initial blue model thicknesses are equal to half the offsets.

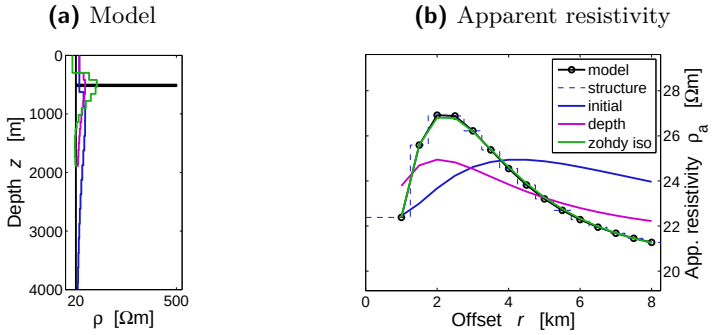

Figure 5.1: Isotropic Zohdy method: The true model with the observed data is given by the black lines. The blue lines show the initial model. The models resulting from the thickness determination and from the complete isotropic Zohdy are given by the purple and the green lines.

The second step determines the layer resistivities

2.1. At every iteration i every layer resistivity $\rho_{j,i}$ is increased (decreased) if the calculated apparent resistivity at the corresponding offset is lower (higher) than the observed apparent resistivity,

$$\rho_{j,i+1} \;=\; \rho_{j,i}\frac{\rho_j^{a,o}}{\rho_{j,i}^{a,c}}\;. \tag{5.2}$$

2.2. Calculate the apparent resistivities for the new model.

2.3. Calculate the new misfit ζ and compare it with the old one.

2.4. Repeat Steps 2.1, 2.2, and 2.3 until the misfit reaches a desired minimum, or the difference between the old and the new misfit falls below a threshold (flattens out), or the calculation reaches a given limit of iterations.

The final model and response after application of the Zohdy method is given by the green lines in Figure 5.1. The depth model yields the same apparent resistivity curve as the observed, black model, and presents another example of non-uniqueness in EM measurements. It is not possible to get more information out of the apparent resistivities.

Loke and Barker (1995) showed two practical improvements to increase the rate of convergence and make the method more stable. Hobbs and Dumitrescu (1997) proposed an adaption to Zohdy's method by using apparent resistivity and phase derived from the magnetotelluric impedance. I propose (a) an expanded Zohdy method to anisotropic data and (b) an improved Zohdy method for isotropic data using apparent anisotropy λ_a in addition to apparent resistivity. Any apparent anisotropy determination explained in Chapter 4 could be used for this expanded Zohdy method. The empirical, analytical peak method apparent anisotropy $\lambda'_{a,p}$, as given in Equation 4.10, is used for the examples in this Chapter.

5.2 Expanded Zohdy method to anisotropic data

Our anisotropic test model has the same layer structure as the isotropic model, the isotropic resistivities ρ are set as the mean resistivities ρ_m, and every layer has anisotropy $\lambda = 2$. Recalling the transverse resistance $\mathcal{R} = \lambda\rho_m d$ indicates that the equivalent isotropic model to this anisotropic model would be placed twice as deep and with double the thickness of this anisotropic model. Applying the standard Zohdy method to this anisotropic data reveals indeed the equivalent isotropic model, as shown in Figure 5.2a: The maximum resistivity amplitude is at roughly 1000 m depth, and the target thickness is much thicker compared to Figure 5.1a.

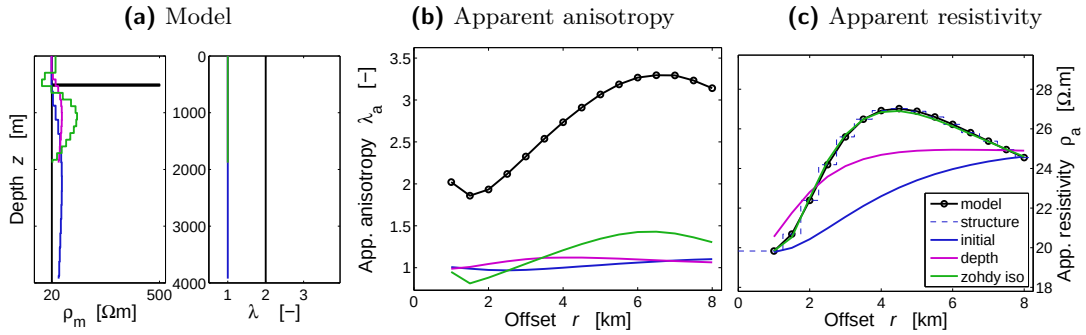

Figure 5.2: Isotropic Zohdy method applied to anisotropic data: The observed model with the measured data is given by the black lines. The blue lines show the initial model. The models resulting from the thickness determination and from the complete isotropic Zohdy are given by the purple and the green lines. The isotropic Zohdy method yields a thick target placed deeper than the real model.

Figure 5.2b shows the apparent resistivity curves for the three stages of the Zohdy method: blue line for the initial model, purple line for the model after the thickness determination, and green line for the complete Zohdy method. It is obvious that the real model and the model from the Zohdy method result in the same apparent resistivity curve, but not in the same apparent anisotropy curve. I expand the Zohdy method by adjusting the apparent anisotropy curve in a manner similar to the resistivity determination.

The third step (anisotropic) determines the layer anisotropies

3a.1. Assume the resistivities ρ from the isotropic Zohdy method are the mean resistivities ρ_m, and the anisotropy for every layer is $\lambda = 1$.

3a.2. Calculate the apparent anisotropy for every offset.

3a.3. Calculate the misfit ζ^a between the measured and the calculated apparent anisotropies,

$$\zeta^a = \sqrt{\frac{1}{N}\sum_{j=1}^{N}\left(\frac{\lambda_j^{a,o} - \lambda_j^{a,c}}{\lambda_j^{a,o}}\right)^2}, \tag{5.3}$$

where N is the number of layers (or offsets), a indicates apparent, and o, c stand for observed and calculated.

3a.4. At every iteration i every layer anisotropy λ_j is increased (decreased) if the calculated apparent anisotropy at the corresponding offset is lower (higher) than the measured apparent anisotropy,

$$\lambda_{j,i+1} \;=\; \lambda_{j,i}\frac{\lambda_j^{a,o}}{\lambda_{j,i}^{a,c}}\;. \tag{5.4}$$

3a.5. At every iteration i every layer thickness d_j is increased (decreased) if the new layer anisotropy is lower (higher) than the old layer anisotropy,

$$d_{j,i+1} \;=\; d_{j,i}\frac{\lambda_{j,i}}{\lambda_{j,i+1}}\;. \tag{5.5}$$

3a.6. Calculate the apparent anisotropy for the new model.

3a.7. Calculate the new misfit ζ^a and compare it with the old one.

3a.8. Repeat steps 3a.4 - 3a.7 until the misfit reaches a desired minimum, or the difference between the old and the new misfit falls below a threshold (flattens out), or the calculation reaches a given limit of iterations.

In Step 3a.5 I make use of constant apparent resistivity for constant transverse resistance $\mathcal{R} = \lambda\rho_m d$, i.e. ensure that the apparent resistivity curve stays constant. This leads, however, to unequal layer thicknesses.

Two layers with thicknesses d', d'', and corresponding horizontal resistivities ρ_h', ρ_h'' and vertical resistivities ρ_v', ρ_v'' behave like a layer with thickness,

$$d \;=\; d' \;+\; d'', \tag{5.6}$$

horizontal resistivity

$$\rho_h \;=\; \frac{\rho_h'\rho_h''(d' \;+\; d'')}{\rho_h'' d' \;+\; \rho_h' d''}\;, \tag{5.7}$$

and vertical resistivity

$$\rho_v \;=\; \frac{\rho_v' d' \;+\; \rho_v'' d''}{d' \;+\; d''}\;, \tag{5.8}$$

as given in, e.g., Maillet (1947). This allows recalculation of the final model into a model with equally thick layers, keeping the apparent anisotropy and apparent resistivity curves constant.

Figure 5.3 shows the result of the expanded anisotropic Zohdy method, given by the orange dashed line. The result is overlaid with the equally layered model in solid red. The anisotropic Zohdy method places the target at the right depth, and determines accurately the overburden anisotropy and resistivity. It succeeds in fitting the apparent anisotropy curve by keeping the apparent resistivity curve constant. The anisotropies, however, are not recovered very well, as they show an anomaly over the target.

Although we double the information by taking apparent resistivity and apparent anisotropy into account, we also double the unknowns of our model, and we cannot expect a better result.

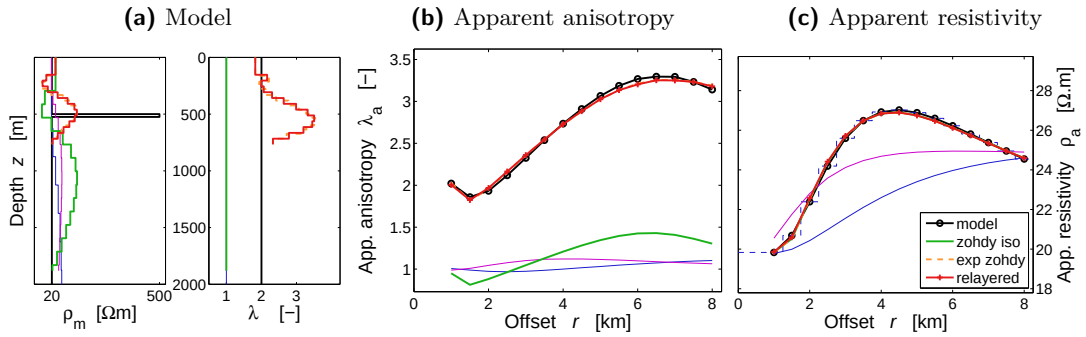

Figure 5.3: Expanded Zohdy method applied to anisotropic data: The observed model with the measured data is given by the black lines. The thin lines show the results form the standard Zohdy method. The orange dashed line shows the result from the anisotropy Zohdy, and is overlaid by the red solid line, the re-layered model with equally thick layers. The anisotropic Zohdy places the target at the right depth, and shows an anisotropy-anomaly over sharp boundaries.

The final model will always be smooth, for the mean resistivity and the anisotropy. Concerning the anisotropy values it has always to be kept in mind that $\lambda = \sqrt{\rho_v/\rho_h}$, and one could plot ρ_h and ρ_v instead of ρ_m and λ, as shown in Figure 5.4. Both, ρ_h and ρ_v, show a smooth resistivity-depth curve, but not the same, as horizontal and vertical resistivities have different sensitivities to different targets. The horizontal resistivity, e.g., is not very sensitive to thin high resistivity targets. These different sensitivities lead to unexpected anisotropy anomalies caused by sharp resistivity boundaries.

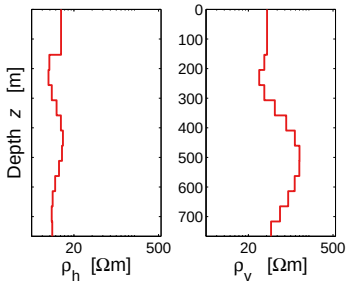

Figure 5.4: Horizontal and vertical resistivities for Figure 5.3: Vertical resistivities are much more sensitive to the high resistivity target than horizontal resistivities.

5.3 Improved Zohdy method for isotropic data

Figure 5.5 shows again the result from the standard Zohdy from isotropic data, with the corresponding apparent anisotropy curves. They show that a finished standard Zohdy does not result in the same apparent anisotropy curve even for isotropic data. This means that the

apparent anisotropy provides information additional to that from apparent resistivity. This can be used to improve the standard Zohdy method.

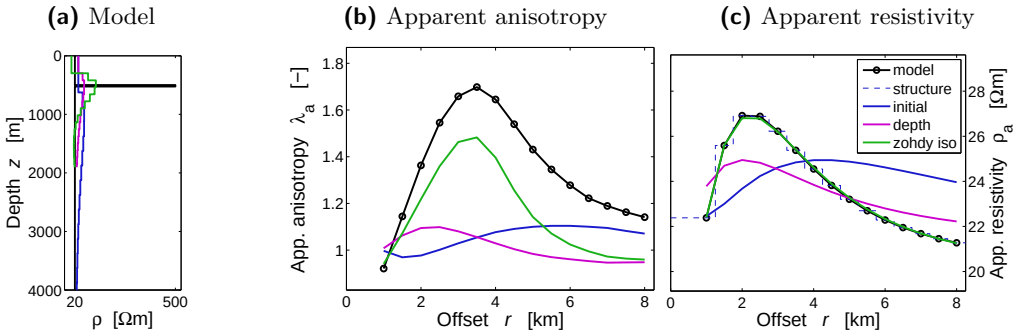

Figure 5.5: Isotropic Zohdy method and apparent anisotropy: (a) and (c) are the results shown in Figure 5.1. The corresponding apparent anisotropy curves are shown in (b). The standard Zohdy method does not satisfy the apparent anisotropy curves.

A stack of isotropic layers appears anisotropic on the surface. The higher the resistivity differences between these layers, the higher is the apparent anisotropy, as can be seen by applying Equations 5.7 and 5.8 to two isotropic layers with $\rho'_h = \rho'_v$ and $\rho''_h = \rho''_v$. I try to match the apparent anisotropy curve in an additional, isotropic step, by adjusting the layer resistivities.

The third step (isotropic) adjusts the apparent anisotropy

3i.1. Calculate the apparent anisotropy for every offset.

3i.2. Calculate the misfit ζ^a between the measured and the calculated apparent anisotropies, Equation 5.3.

3i.3. At every iteration i every layer resistivity ρ_j is increased (decreased) if the calculated apparent anisotropy at the corresponding offset is lower (higher) than the measured apparent anisotropy,

$$\rho_{j,i+1} \;=\; \rho_{j,i} \frac{\lambda_j^{a,o}}{\lambda_{j,i}^{a,c}} \;. \tag{5.9}$$

3i.4. At every iteration i every layer thickness d_j is increased (decreased) if the new layer resistivity is lower (higher) than the old layer resistivity,

$$d_{j,i+1} \;=\; d_{j,i} \frac{\rho_{j,i}}{\rho_{j,i+1}} \;. \tag{5.10}$$

3i.5. Calculate the apparent anisotropy for the new model.

3i.6. Calculate the new misfit ζ^a and compare it with the old one.

3i.7. Repeat steps 3i.3 - 3i.6 until the misfit reaches a desired minimum, or the difference between the old and the new misfit falls below a threshold (flattens out), or the calculation reaches a given limit of iterations.

3i.8. Carry out a resistivity adjustment as explained (second step of the isotropic Zohdy method).

Figure 5.6 shows the result from the improved Zohdy scheme. It can clearly narrow the target and increase the target resistivity. The brown curve is the result after the adjustments to the apparent anisotropy curve, and the final red curve is the result after the resistivity adjustments, Step 3i.8. The calculated apparent anisotropy curve does recover well the measured apparent anisotropy curve after this additional iteration. This iteration scheme could, however, be repeated iteratively itself, to yield a better result. It takes a long time to achieve a satisfying fit for both apparent resistivity and apparent anisotropy, as it converges very slowly.

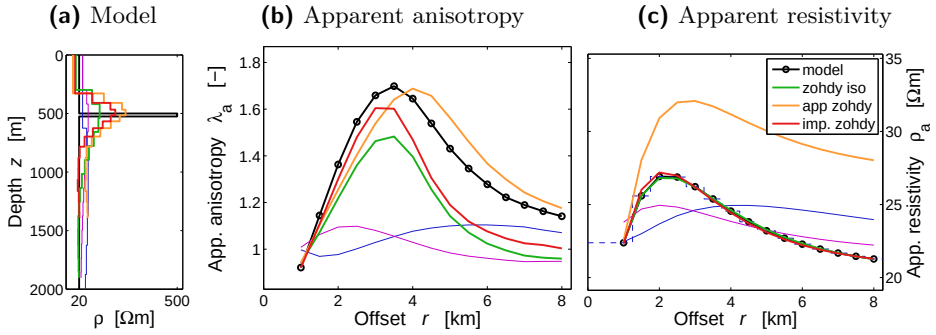

Figure 5.6: Improved Zohdy method for isotropic data: One additional iteration loop improves the fit of the calculated with the measured apparent anisotropy curve, and narrows down the target.

Summary

The Zohdy method yields in a fast iterative way a $1\mathcal{D}$ resistivity model from apparent resistivities of multiple offsets. I showed that including apparent anisotropies for every offset can either improve the Zohdy method for isotropic data or extend the Zohdy method to anisotropic data. Horizontal and vertical resistivities are not equally sensitive to high resistivity targets, resulting in anisotropy anomalies over sharp resistivity boundaries.

6

Inversion

Determining subsurface resistivities and anisotropies

The standard $1\mathcal{D}$ processing tool for MTEM data in PGS EM is full waveform inversion. The inversion routine is a Fortran code called `MTEM1D_INV`, and can handle land step and impulse responses and marine impulse responses for both single and multi-offsets. It has a variety of different inversions included, e.g. Occam inversion or ridge regression. Specific flags can be set to, e.g., exclude one or more layers from the constraints, or fix the resistivity of one or more layers.

I included anisotropy in two different ways into the exisiting inversion, first as a fixed parameter, and second as a free parameter. Every layer anisotropy must be provided for a fixed anisotropic inversion, and the inversion inverts then for the mean resistivity ρ_m. In the free anisotropic inversion it inverts for both ρ_h and ρ_v separately.

6.1 MTEM1D_INV

The purpose of any inversion is to find the best fitting model to some data, where 'best fitting' in general means minimising a misfit function. The data in our case are either step or impulse MTEM responses, a set of discrete time points with corresponding amplitude values. The model we are looking for is a $1\mathcal{D}$ horizontally layered model with a corresponding resistivity value ρ in the isotropic case, or two resistivity values ρ_h and ρ_v in the anisotropic case, for each layer.

The inversion of electromagnetic sounding data is a highly non-linear and non-unique problem. For this reason Constable et al. (1987) proposed a linearised inversion algorithm which searches for the simplest or smoothest model, the Occam inversion (according to Occam's razor, the principle that "entities should not be multiplied unnecessarily"). The Jacobian matrix for each iteration is found by calculating the change of the response at each data point for a small change in the resistivity value(s) of each layer. The inversion finds a solution vector $\delta\mathbf{d}$ at every iteration, which is used to adjust the initial model resistivity values. The derivation of the Jacobian, the misfit χ^2, the solution vector and a stabilising function are derived for the anisotropic case in Appendix A. Appendix D lists the necessary additional information to the user guide for the anisotropic inversions.

The inversion makes use of two different forward modellers, which are described in Section 3.2. `MTEM1D_INV` has many more possibilities than the above mentioned Occam inversion, and can also handle layers free from any constraints, layers with fixed resistivities, or invert combined for layer resistivities and layer thicknesses. Also damping and weighting can be applied, or a specific structure-model can be supplied.

Every method has it advantages and disadvantages, and depending on the model one or the other works better, which is often a subjective decision, if two different models satisfy the input data. It is, however, not my intention to show the best inversion results that are possible with `MTEM1D_INV`, which would already start in defining a good detectable target. My ambition is more to show with a simple model and a few parameters, which are described further down, the effects of anisotropy on the inversion. I hope to make the reader aware of the possibilities and limitations of anisotropic inversion, which should help in interpretation of complex models when inverting fully anisotropic.

The effects of anisotropy on the inversion are illustrated by answering three constitutive questions:

1. What does an isotropic inversion with isotropic and anisotropic input data result in (Section 6.2)?
2. How can a good estimate of the subsurface anisotropy coefficients, provided as fixed parameters to the inversion, improve the result (Section 6.3)?
3. What does an anisotropic inversion with anisotropic input data result in (6.4)?

Technical parameters for the inversion

All inversions in this chapter are carried out with the above cited standard Occam inversion. In this regularised inversion the regularisation parameter μ controls the degree of smoothness. Its optimum value is found through a search to find the minimum data misfit for each different value of μ within each iteration. I used in all cases a range search method, which searches for the smallest misfit χ^2 for a range of different values of μ between 1×10^{-4} and 1×10^{3}.

If not otherwise stated the following parameters were applied to all isotropic (anisotropic) inversions: 40 (80) logarithmic equally spaced data-points are given, the first one at one millisecond. Care was taken that at least 10 (20) data-points were provided before the arrival time of the peak, and that the last data-point reached five times the time of the peak. The inversion was always run with 21 equally spaced layers, and the depth was set to 50 % (50 %/λ) of the offset, or of the largest offset in multi-offset inversions.

The starting model is calculated by `MTEM1D_INV`, a fast iterative routine using the analytical solution for a uniform VTI half-space to find the best fitting isotropic (anisotropic) half-space.

The parameter weighting and data weighting options, given in Equations A-16 and A-17, are always switched on. Two of the stop criteria, the maximum number of iterations and the minimum misfit χ^2, are set to unrealistically high (50) and low (1×10^{-3}) values, to see whether the inversion converges by flattening out, or because the misfit increases. Any misfit $\chi^2 < 1$ is regarded as an acceptable inversion result.

Inversions for a range of offsets are carried out, and the three results with the lowest misfit are shown and used for a multi-offset inversion.

All inversions are carried out for land step responses. Anisotropy, however, is included for both land step and impulse and marine impulse responses. The results presented apply equally to land and marine impulse responses.

6.2 Isotropic inversion of isotropic and anisotropic data

Figure 6.1a shows a typical isotropic inversion result from `MTEM1D_INV` over our standard model (described in Section 2.2), for three different offsets, and a combined inversion of these three offsets. The inversion recovers overburden resistivity, target depth and transverse resistance of the target, and even a good estimate of the underburden. Figure 6.1b shows the input data and the calculated responses from the inversion model for the combined inversion, as an example.

What happens when we invert anisotropic data isotropically? An insightful result is shown in Figure 6.2a, the isotropic inversion of a uniform VTI half-space. The model (black line) is a uniform VTI half-space with anisotropy $\lambda = 2$, and mean resistivity $\rho_m = 20$ Ωm. An isotropic inversion yields, independent of the offset, a near-surface resistivity of 10 Ωm, and creates a massive target, whose depth is dependent on the offset. A combined inversion fails. What is the reason for this behaviour? We have seen in Section 3.3 that the airwave is only dependent on the horizontal resistivity. But also the earth response from the near surface is predominantly dependent on the horizontal resistivity, as the offset r is much larger than the penetration depth.

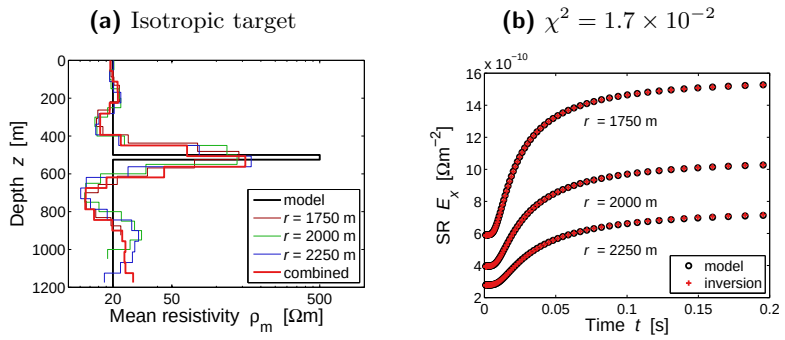

Figure 6.1: Isotropic inversion of isotropic data: overburden, target depth, target transverse resistance and underburden are nicely recovered. The fit between input data and inversion result is shown in (b)

The inversion fits therefore the horizontal resistivity of the input data, which is $\rho_m/\lambda = 10\ \Omega$m. To reach the same late-time value as the input model it creates a high resistivity target, which is put at different depths depending on the offset.

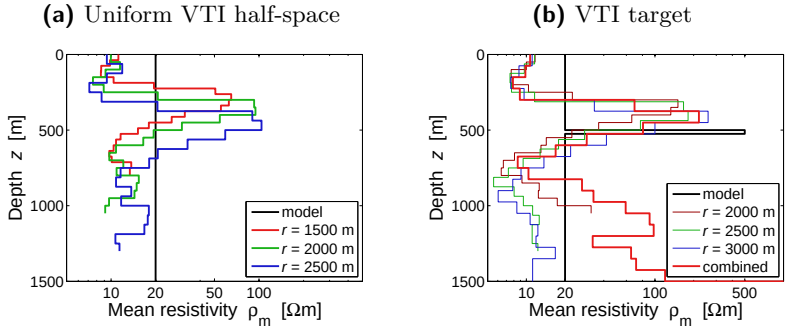

Figure 6.2: Isotropic inversion of anisotropic data: (a) a uniform VTI half-space with $\lambda = 2$, and (b) an anisotropic target model with $\lambda = 2$ for every layer.

The isotropic inversion of an anisotropic target, shown in Figure 6.2b shows similar characteristics as we have seen for a half-space. The near-surface approximates the horizontal resistivity of the anisotropic input model. In addition, the target depth location is offset dependent: The depth of the two layers with the highest resistivity values are increasing with increasing offset. The combined inversion fails to find a satisfying result and flattens out at $\chi^2 = 1.21$. Multi-offset inversions for real data often fail, and I suspect anisotropy to be one reason which causes a failure.

6.3 Anisotropy as a fixed parameter

Assuming that we have a good estimate of the subsurface anisotropy, e.g. well logs, we can carry out an inversion with fixed anisotropies. Figure 6.3 shows the result for the same model as used for the isotropic inversion of anisotropic data: a target with $\rho_m = 500$ Ωm in a background of $\rho_m = 20$ Ωm, all layers having an anisotropy coefficient of $\lambda = 2$. The inversion result, where now all layers have as well an anisotropy coefficient of $\lambda = 2$, is comparable with the isotropic inversion result of isotropic data: The inversion reveals very accurate overburden and underburden resistivities, places the target at the correct depth and gives a good estimate of the transverse resistance of the target. Note that the isotropic target in Figure 6.1a is not the equivalent model of the anisotropic target in Figures 6.2b and 6.3, as the transverse resistance $\mathcal{R} = \lambda\rho_m d$ is not the same.

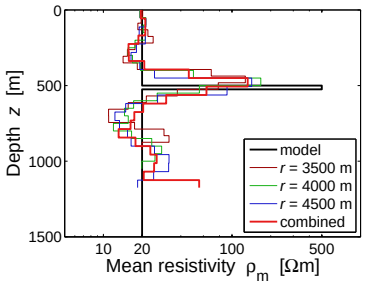

Figure 6.3: Inversion with fixed anisotropies: the result is comparable to an isotropic inversion of isotropic data. Overburden, target depth, target transverse resistance and underburden are nicely recovered.

This result is expected, as an anisotropic inversion with fixed anisotropies does basically the same as an isotropic inversion; the unknowns and the degree of freedom is the same.

6.4 Anisotropy as a free parameter

The result for the same model, but inverted for free anisotropies, is shown in Figure 6.4b. It is both disillusioning and encouraging. The inversion for offset $r = 4.5$ km (blue curve) is a good example of the almost unlimited non-uniqueness. The misfit falls below 1×10^{-3} in just five iterations, and it has not significantly changed from the initial best fitting starting half-space. It is encouraging that a combined inversion reveals accurately overburden and underburden resistivities and anisotropies, and places the target, although very smooth, at about the right depth.

Some very important conclusions can be found by analysing Figure 6.4c.

- The horizontal resistivities of the shallow subsurface are very well recovered for every offset. The vertical resistivities, on the other hand, are not really sensitive to the near surface and can vary a lot. This is in agreement with our observations from isotropic inversions of anisotropic data.

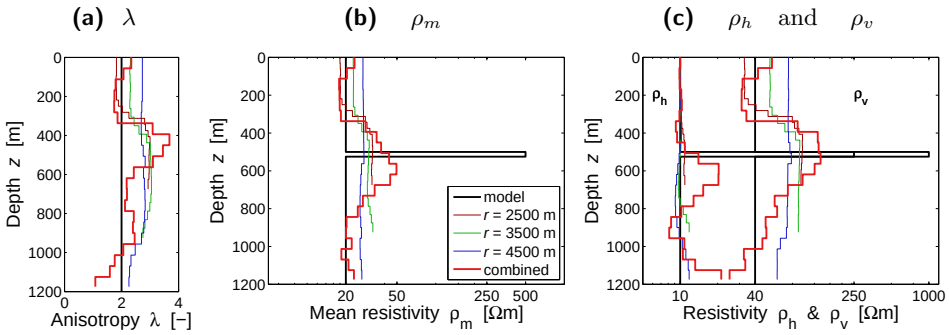

Figure 6.4: Anisotropic inversion of anisotropic data: Single offset inversions are not sufficient to recover the model. Horizontal and vertical resistivities are sensitive to different features, leading to anisotropy anomalies.

- Horizontal resistivities are, in single offset inversions, not sensitive to thin changes, even if they are as strong as our target in the model.
- Horizontal resistivities do reveal thin changes in multi-offset inversions. But these are out of phase (deeper) compared to vertical resistivities.
- This different sensitivity of horizontal and vertical resistivity causes unexpected high anisotropy anomalies at strong resistivity boundaries, as shown in Figure 6.4a.

These insights are very important, and I want to emphasise them by simplifying our model and inverting for a step model, as shown in Figure 6.5. Again, the horizontal resistivities of the near surface are recovered accurately, the vertical resistivities show more variability. It shows that the horizontal resistivities are affected by changes even in single offset inversion, if the layer is thick enough. But the detection of the resistivity change by the horizontal resistivity is out of phase compared to the vertical resistivity, which causes an anisotropy anomaly at the boundary. (This is only well seen in the combined inversion, as the single offset inversions have too much freedom in the overburden vertical resistivity.)

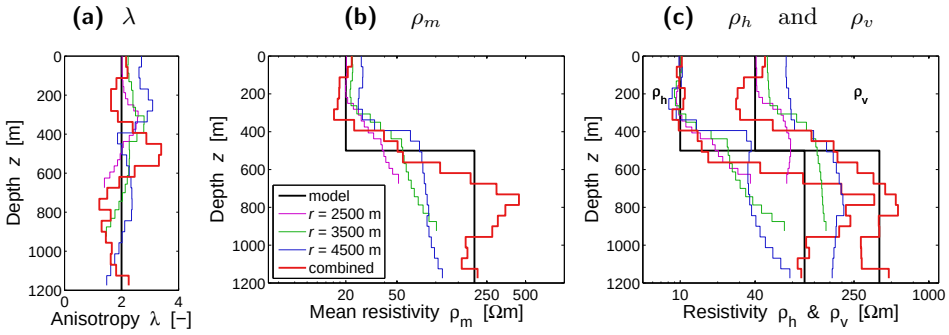

Figure 6.5: Anisotropic inversion of a step-model: Sharp resistivity boundaries cause anisotropy anomalies, as the horizontal and vertical resistivities do not detect the change at the same depth.

Having in mind the effects of sharp resistivity boundaries we can have another look at Figure 6.4: After the first six layers the vertical resistivity shows a sudden increase, whereas the horizontal resistivity remains almost unchanged, causing a jump in the anisotropy curve. We relate this to a sharp resistivity change, and assume the first six layers to be an accurate presentation of the overburden. Averaging the mean resistivities of the first six layers (23.5, 20.4, 17.7, 17.9, 17.9, and 18.3 Ωm) yields an overburden mean resistivity of $\rho_m = 19.3$ Ωm. The corresponding overburden anisotropy is $\lambda = 1.93$ (2.34, 2.07, 1.79, 1.75, 1.74, 1.86). These values could be used as fixed anisotropy values for a fixed inversion, as shown in Section 6.3. Such a combination of free anisotropic inversion for a background estimation, followed by a fixed anisotropic inversion, could be used to improve the result.

Summary

I have shown that an isotropic inversion of anisotropic data struggles to define the correct target depth, and fails for multi-offset inversions. Isotropic inversions approximate the horizontal resistivity of an anisotropic input for the near surface, and compensate deeper in the model for the missing resistivity. Single offset free anisotropic inversions are not sufficient to delineate any target, the non-uniqueness is too big. Horizontal resistivities are not sensitive to thin resistivity changes. This shortcoming can be accounted for by inverting for multi-offsets. But horizontal resistivity anomalies are detected later than vertical resistivity anomalies, causing anisotropy anomalies over sharp resistivity boundaries.

7

Conclusions

7.1 Anisotropy in EM

The huge effects of resistivity anisotropy have been known for almost as long as there have been resistivity measurements. The isotropic assumption is, however, still applied in most cases. One reason is that the increase in non-uniqueness is dramatic if VTI is considered, even more for TI, and is suspected to be literally unlimited if general anisotropy is taken into account.

Conventional DC measurements do not allow us to distinguish between different subsurface anisotropies. Anisotropic subsurfaces yield the same DC values as the equivalent isotropic subsurfaces. But the depth of investigation is different, which makes it hard to locate target depths correctly.

7.2 Anisotropy in MTEM

MTEM data contain more information than conventional DC measurements, and they recover more details from the subsurface. Apparent anisotropy curves can serve as a first indication for the presence of anisotropy.

Free anisotropic inversions do not necessarily result in satisfying models. There are, in my opinion, two main reasons causing poor anisotropic inversion results: First the non-uniqueness in VTI is too big. For any measured step response there is an anisotropic half-space satisfying the initial step and the late-time value with the horizontal resistivity of the near surface and an appropriate anisotropy coefficient. There is often not much of a change needed to this initial half-space to fit the measured response. And second the horizontal resistivity is not sensitive to thin resistivity changes, even if they are high. Vertical resistivity detects a change in resistivity always shallower than the horizontal resistivity, which causes anisotropy anomalies.

I do believe, however, that the combination of the available tools results in better resistivity models than purely isotropic inversions. Comparison of isotropic and free anisotropic inversion results give an insight into the present anisotropies and can be used to determine a good background model. Inverting with a good background model and fixed anisotropies yields the quality of inversion results we are used to from isotropic inversions. It will, however, always be a question of experience and knowledge from the geophysicist who is carrying out the inversions. But this is not a change in current practice at all.

7.3 Outlook

Study and analysis of anisotropy must stay a high-priority task, despite or because of the big problems the non-uniqueness is causing. The effects of anisotropy are too significant to be neglected. One possibility is to decrease the non-uniqueness by including additional resistivity information, such as borehole resistivity data, or structural information from seismic data. Measuring additional to the E_x component a magnetic component or the cross-line component E_y would decrease the problem of non-uniqueness as well, as more data are provided.

An interesting test would be to apply the anisotropic inversion code to measured data sets, where isotropic inversions have been carried out already. Comparing the isotropic results with the anisotropic results might yield some information on the robustness of the code and give some additional insights into the subsurface.

Another interesting task will be to investigate anisotropy in the ongoing work for $3\mathcal{D}$ inversion of MTEM data, and also to investigate anisotropy for a towed system, where the signal first travels through an always isotropic water column, and then enters the anisotropic subsurface.

An expansion in another direction would be to investigate as a next step into general TI for structure with dipping layer formations, e.g., deltaic sediments.

A

Theoretical derivation

Linearised inversion including anisotropy

The inversion code `MTEM1D_INV` inverts MTEM step and impulse responses to a $1\mathcal{D}$ resistivity model, as shown in Chapter 6. Inversion of MTEM responses is a non-linear problem and hence must be linearised. The linearised inversion is then solved iteratively, which requires the calculation of the so-called Jacobian matrices for each iteration.

An isotropic inversion for N layers has a model vector of length N with corresponding Jacobian matrices of size $M \times N$, where M is the number of measured data points. Extending the inversion to VTI gives a model vector of length $2N$ with corresponding Jacobian matrices of size $M \times 2N$.

The routine `stabilise` prevents the layer anisotropies changing too dramatically in a single iteration by restricting the maximum change to a quarter of the current mean resistivity. Data and parameter weighting are optional constraints.

A.1 Jacobian

Our model consists of N layers and is parameterised by the horizontal and vertical resistivities for every layer, ρ_i^h and ρ_i^v respectively, where $i \in \{1, N\}$ (h and v being superscripts in this Chapter). The *model vector* $\mathbf{m}$ is therefore a vector with size $2N \times 1$,

$$\mathbf{m}^\mathsf{T} \;=\; [\rho_1^h, \rho_2^h, \ldots, \rho_N^h,\; \rho_1^v, \rho_2^v, \ldots, \rho_N^v] \;. \tag{A-1}$$

Every measured data d_j with $j \in \{1, M\}$ is put into a *data vector* $\mathbf{d}^{\text{meas}}$ ($M \times 1$),

$$(\mathbf{d}^{\text{meas}})^\mathsf{T} \;=\; [d_1, d_2, \ldots, d_M] \;. \tag{A-2}$$

We can compute the response $\mathbf{d}^{\text{calc}}$ for given parameters with a *forward model* $\mathbf{F}$,

$$\mathbf{d}^{\text{calc}} \;=\; \mathbf{F}[\mathbf{m}] \;. \tag{A-3}$$

Our forward model is a non-linear function. We linearise it by proposing a starting *guess model* $\mathbf{m}_g$, assuming that $\mathbf{F}$ is differentiable at $\mathbf{m}_g$,

$$\mathbf{F}[\mathbf{m}_g \;+\; \delta\mathbf{m}] \;=\; \mathbf{F}[\mathbf{m}_g] \;+\; \left(\frac{\partial \mathbf{F}}{\partial \mathbf{m}}\right)_{m_g} \delta\mathbf{m} \;+\; \text{higher orders (neglected)} \;. \tag{A-4}$$

To improve our guess model we seek to minimise the scalar *objective function* χ^2,

$$\chi^2 \;=\; \|\mathbf{d}^{\text{meas}} \;-\; \mathbf{F}[\mathbf{m}_g \;+\; \delta\mathbf{m}]\|^2 \;, \tag{A-5}$$

where $\|\cdot\|$ is the Euclidean distance. In index notation, except for the guess model $\mathbf{m}_g$, χ^2 is given by

$$\begin{aligned}
\chi^2 \;&=\; \sum_{j=1}^{M} \left\{ d_j^{\text{meas}} \;-\; \left[F_j[\mathbf{m}_g] \;+\; \sum_{i=1}^{2N} \left(\frac{\partial F_j}{\partial m_i}\right)_{m_g} \delta m_i \right] \right\}^2 \\
&=\; \sum_{j=1}^{M} \left\{ \delta d_j \;-\; \sum_{i=1}^{2N} J_{ji} \delta m_i \right\}^2 \\
&=\; \sum_{j=1}^{M} \left\{ \delta d_j \;-\; \left(\frac{\partial F_j}{\partial \rho_1^h}\right)_{m_g} \delta\rho_1^h \;-\; \cdots \;-\; \left(\frac{\partial F_j}{\partial \rho_N^h}\right)_{m_g} \delta\rho_N^h \right. \\
&\qquad \left. -\; \left(\frac{\partial F_j}{\partial \rho_1^v}\right)_{m_g} \delta\rho_1^v \;-\; \cdots \;-\; \left(\frac{\partial F_j}{\partial \rho_N^v}\right)_{m_g} \delta\rho_N^v \right\}^2 ,
\end{aligned} \tag{A-6}$$

where the difference of the measured data and the guess model is written as

$$\delta\mathbf{d} \;=\; \mathbf{d}^{\text{meas}} \;-\; \mathbf{F}[\mathbf{m}_g] \;, \tag{A-7}$$

and the derivatives of every data point $F_j[\mathbf{m}_g]$ with respect to every parameter m_i is given by the Jacobian $\mathbf{J}$ with size $M \times 2N$,

$$J_{ji} \;=\; \left(\frac{\partial F_j}{\partial m_i}\right)_{m_g} \;=\; \begin{bmatrix} \left(\frac{\partial F_1}{\partial \rho_1^h}\right)_{m_g} & \cdots & \left(\frac{\partial F_1}{\partial \rho_N^h}\right)_{m_g} & \left(\frac{\partial F_1}{\partial \rho_1^v}\right)_{m_g} & \cdots & \left(\frac{\partial F_1}{\partial \rho_N^v}\right)_{m_g} \\ \vdots & \ddots & \vdots & \vdots & \ddots & \vdots \\ \left(\frac{\partial F_M}{\partial \rho_1^h}\right)_{m_g} & \cdots & \left(\frac{\partial F_M}{\partial \rho_N^h}\right)_{m_g} & \left(\frac{\partial F_M}{\partial \rho_1^v}\right)_{m_g} & \cdots & \left(\frac{\partial F_M}{\partial \rho_N^v}\right)_{m_g} \end{bmatrix} . \tag{A-8}$$

We minimise the objective function by differentiating χ^2 with respect to the unknowns $\delta\mathbf{m}$,

$$\frac{\partial \chi^2}{\partial \delta m_q} \;=\; 2\sum_{j=1}^{M}\left\{\delta d_j \;-\; \sum_{i=1}^{2N} J_{ji}\delta m_i\right\}(-J_{jq}) \;=\; 0\;, \qquad \text{for all} \quad q \in \{1, 2N\}\;. \tag{A-9}$$

Equation A-9 can be rearranged and rewritten in vector notation to yield the so-called *normal equations*,

$$\left[\mathbf{J}^\mathsf{T}\mathbf{J}\right]\delta\mathbf{m} \;=\; \mathbf{J}^\mathsf{T}\delta\mathbf{d}\;, \tag{A-10}$$

Solving the normal equations for the *solution vector* $\delta\mathbf{m}$,

$$\delta\mathbf{m} \;=\; \left[\mathbf{J}^\mathsf{T}\mathbf{J}\right]^{-1}\mathbf{J}^\mathsf{T}\delta\mathbf{d}\;, \tag{A-11}$$

allows us to update our initial guess model $\mathbf{m}_g$

$$\mathbf{m}_g^{\text{new}} \;=\; \mathbf{m}_g^{\text{old}} \;+\; \delta\mathbf{m}\;. \tag{A-12}$$

We now write out the normal equations in more detail and derive the q^{th} equation, omitting in the following the explicit declaration $(\cdot)_{m_g}$ for better readability. From Equation A-10 it follows that

$$\sum_{i=1}^{2N}\sum_{j=1}^{M}\frac{\partial F_j}{\partial m_q}\frac{\partial F_j}{\partial m_i}\delta m_i \;=\; \sum_{j=1}^{M}\frac{\partial F_j}{\partial m_q}\delta d_j\;, \qquad \text{for all} \quad q \in \{1, 2N\}\;, \tag{A-13}$$

and the left and right hand sides of the q^{th} equation are given by

$$\begin{aligned} \text{LHS} \;=\; &\left[\frac{\partial F_1}{\partial m_q}\frac{\partial F_1}{\partial \rho_1^h} \;+\; \cdots \;+\; \frac{\partial F_M}{\partial m_q}\frac{\partial F_M}{\partial \rho_1^h}\right]\delta\rho_1^h \quad + \cdots + \\ &\left[\frac{\partial F_1}{\partial m_q}\frac{\partial F_1}{\partial \rho_N^v} \;+\; \cdots \;+\; \frac{\partial F_M}{\partial m_q}\frac{\partial F_M}{\partial \rho_N^v}\right]\delta\rho_N^v \end{aligned} \tag{A-14}$$

$$\text{RHS} \;=\; \frac{\partial F_1}{\partial m_q}\left\{d_1^{\text{meas}} \;-\; F_1[\mathbf{m}_g]\right\} \;+\; \cdots \;+\; \frac{\partial F_M}{\partial m_q}\left\{d_1^{\text{meas}} \;-\; F_M[\mathbf{m}_g]\right\}\;. \tag{A-15}$$

The complete normal equations for all q are given on Page 77.

Normal Equations

$$
\begin{pmatrix}
\left[\frac{\partial F_1}{\partial \rho_1^h}\frac{\partial F_1}{\partial \rho_1^h}\right] & \cdots & \left[\frac{\partial F_1}{\partial \rho_1^h}\frac{\partial F_1}{\partial \rho_N^h}\right] & \left[\frac{\partial F_1}{\partial \rho_1^h}\frac{\partial F_1}{\partial \rho_1^v}\right] & \cdots & \left[\frac{\partial F_1}{\partial \rho_1^h}\frac{\partial F_1}{\partial \rho_N^v}\right] & \cdots & \left[\frac{\partial F_1}{\partial \rho_1^h}\frac{\partial F_M}{\partial \rho_N^v}\right] \\
\vdots & \ddots & \vdots & \vdots & \cdots & \vdots & \ddots & \vdots \\
\left[\frac{\partial F_1}{\partial \rho_N^h}\frac{\partial F_1}{\partial \rho_1^h}\right] & \cdots & \left[\frac{\partial F_1}{\partial \rho_N^h}\frac{\partial F_1}{\partial \rho_N^h}\right] & \left[\frac{\partial F_1}{\partial \rho_N^h}\frac{\partial F_1}{\partial \rho_1^v}\right] & \cdots & \left[\frac{\partial F_1}{\partial \rho_N^h}\frac{\partial F_1}{\partial \rho_N^v}\right] & \cdots & \left[\frac{\partial F_1}{\partial \rho_N^h}\frac{\partial F_M}{\partial \rho_N^v}\right] \\
\left[\frac{\partial F_1}{\partial \rho_1^v}\frac{\partial F_1}{\partial \rho_1^h}\right] & \cdots & \left[\frac{\partial F_1}{\partial \rho_1^v}\frac{\partial F_1}{\partial \rho_N^h}\right] & \left[\frac{\partial F_1}{\partial \rho_1^v}\frac{\partial F_1}{\partial \rho_1^v}\right] & \cdots & \left[\frac{\partial F_1}{\partial \rho_1^v}\frac{\partial F_1}{\partial \rho_N^v}\right] & \cdots & \left[\frac{\partial F_1}{\partial \rho_1^v}\frac{\partial F_M}{\partial \rho_N^v}\right] \\
\vdots & \ddots & \vdots & \vdots & \cdots & \vdots & \ddots & \vdots \\
\left[\frac{\partial F_1}{\partial \rho_N^v}\frac{\partial F_1}{\partial \rho_1^h}\right] & \cdots & \left[\frac{\partial F_1}{\partial \rho_N^v}\frac{\partial F_1}{\partial \rho_N^h}\right] & \left[\frac{\partial F_1}{\partial \rho_N^v}\frac{\partial F_1}{\partial \rho_1^v}\right] & \cdots & \left[\frac{\partial F_1}{\partial \rho_N^v}\frac{\partial F_1}{\partial \rho_N^v}\right] & \cdots & \left[\frac{\partial F_1}{\partial \rho_N^v}\frac{\partial F_M}{\partial \rho_N^v}\right] \\
\vdots & \ddots & \vdots & \vdots & \cdots & \vdots & \ddots & \vdots \\
\left[\frac{\partial F_M}{\partial \rho_1^h}\frac{\partial F_1}{\partial \rho_1^h}\right] & \cdots & \left[\frac{\partial F_M}{\partial \rho_1^h}\frac{\partial F_1}{\partial \rho_N^h}\right] & \left[\frac{\partial F_M}{\partial \rho_1^h}\frac{\partial F_1}{\partial \rho_1^v}\right] & \cdots & \left[\frac{\partial F_M}{\partial \rho_1^h}\frac{\partial F_1}{\partial \rho_N^v}\right] & \cdots & \left[\frac{\partial F_M}{\partial \rho_1^h}\frac{\partial F_M}{\partial \rho_N^v}\right] \\
\vdots & \ddots & \vdots & \vdots & \cdots & \vdots & \ddots & \vdots \\
\left[\frac{\partial F_M}{\partial \rho_N^h}\frac{\partial F_1}{\partial \rho_1^h}\right] & \cdots & \left[\frac{\partial F_M}{\partial \rho_N^h}\frac{\partial F_1}{\partial \rho_N^h}\right] & \left[\frac{\partial F_M}{\partial \rho_N^h}\frac{\partial F_1}{\partial \rho_1^v}\right] & \cdots & \left[\frac{\partial F_M}{\partial \rho_N^h}\frac{\partial F_1}{\partial \rho_N^v}\right] & \cdots & \left[\frac{\partial F_M}{\partial \rho_N^h}\frac{\partial F_M}{\partial \rho_N^v}\right]
\end{pmatrix}
\begin{pmatrix}
\delta\rho_1^h \\ \cdots \\ \delta\rho_N^h \\ \delta\rho_1^v \\ \cdots \\ \delta\rho_N^v
\end{pmatrix}
$$

$$
=
$$

$$
\begin{pmatrix}
\frac{\partial F_1}{\partial \rho_1^h} & \cdots & \frac{\partial F_M}{\partial \rho_1^h} \\
\vdots & \ddots & \vdots \\
\frac{\partial F_1}{\partial \rho_N^h} & \cdots & \frac{\partial F_M}{\partial \rho_N^h} \\
\frac{\partial F_1}{\partial \rho_1^v} & \cdots & \frac{\partial F_M}{\partial \rho_1^v} \\
\vdots & \ddots & \vdots \\
\frac{\partial F_1}{\partial \rho_N^v} & \cdots & \frac{\partial F_M}{\partial \rho_N^v}
\end{pmatrix}
\begin{pmatrix}
d_1^{\text{meas}} - F_1[\mathbf{m}_g] \\ \cdots \\ d_M^{\text{meas}} - F_M[\mathbf{m}_g]
\end{pmatrix}
$$

A.2 Parameter and data weighting

Parameter weighting $\mathbf{w}^p$ and data weighting $\mathbf{w}^d$ may be applied following Zhdanov (2002) and using above notations, given by

$$w_i^p = \left[\frac{\sum_{j=1}^{M} J_{ij}^2}{\sum_{j=1}^{M} J_{1j}^2}\right]^{1/4} , \tag{A-16}$$

and

$$w_j^d = \left[\frac{\sum_{i=1}^{2N} J_{ji}^2}{\sum_{i=1}^{2N} J_{1i}^2}\right]^{1/2} . \tag{A-17}$$

A.3 Stabilise

`MTEM1D_INV` makes use of a routine called `stabilise`, to make sure that adjacent layer resistivities do not change too extremely in a single iteration. This routine was, as the name suggests, introduced to stabilise the inversion. For the isotropic inversion this routine is given by

$$\delta\rho_i = \begin{cases} \delta\rho_i & \text{if} \quad |\delta\rho_i| \leq \dfrac{\rho_i}{4} \\ \dfrac{|\delta\rho_i|}{\delta\rho_i}\dfrac{\rho_i}{4} & \text{if} \quad |\delta\rho_i| > \dfrac{\rho_i}{4} \end{cases} , \tag{A-18}$$

for every layer i.

For the anisotropic inversion the stabilise routine compares the changes in ρ^h and ρ^v to the mean resistivity,

$$\delta\rho_i^{h,v} = \begin{cases} \delta\rho_i^{h,v} & \text{if} \quad |\delta\rho_i^{h,v}| \leq \dfrac{\sqrt{\rho_i^h \rho_i^v}}{4} \\ \dfrac{|\delta\rho_i^{h,v}|}{\delta\rho_i^{h,v}}\dfrac{\rho_i^m}{4} & \text{if} \quad |\delta\rho_i^{h,v}| > \dfrac{\sqrt{\rho_i^h \rho_i^v}}{4} \end{cases} . \tag{A-19}$$

B

TE-mode and TM-mode

Separation of TE-mode and TM-mode

EM waves are a superposition of two modes of propagation termed transverse magnetic and transverse electric with different characteristics. Analysing the two different modes separately can yield additional information about the subsurface. Decomposing measured signals into the two different modes is not an easy task. It is, however, possible to model them for VTI.

B.1 Uniform VTI half-space

The electromagnetic signal measured by MTEM is a superposition of the Transverse Electric (TE) mode and the Transverse Magnetic (TM) mode. The TE-mode has no electric field in the direction of propagation, whereas the TM-mode has no magnetic field in the direction of propagation. The galvanic source generates both modes, which then propagate uncoupled through the medium.

The TE-mode is sometimes also called Tangential Electric mode, or Poloidal Magnetic mode (PM-mode). The TM-mode is accordingly termed Tangential Magnetic or Toroidal Magnetic mode.

Electromagnetic coupling between adjacent layers is inductive in the TE-mode, whereas it is galvanic in the TM-mode. The airwave is a pure TE-mode (Weidelt, 2007), as there is no charge flow from the subsurface to the air (continuity along the interface). The TE-mode, due to the inductive coupling, is much less affected by a thin horizontal high resistivity hydrocarbon target than the TM-mode. Separate analyses would help to improve the interpretation of EM measurements, provided that the two modes can be decomposed. Nordskag et al. (2007) showed an approach to decompose the modes for CSEM data by using horizontal gradients.

To date, however, there has been no attempt to decompose TE-mode and TM-mode in MTEM data. Our forward modeller `MTEM1D` (see Section 3.2) calculates both modes separately, and adds them up for the total response. It is therefore possible to plot the two different modes. Figure B.1 shows the decomposed modes for the step responses given in Figure 3.1. It shows that, for a uniform VTI half-space, the TE-mode is only dependent on the horizontal resistivity, and goes to zero for $t \to \infty$. The physical reason is that the TE-mode is an induced field. This vanishes in the static state, as there is no change in the magnetic field anymore. The TM-mode, on the other hand, depends only on the horizontal resistivity in the beginning, and purely on the mean resistivity for $t \to \infty$.

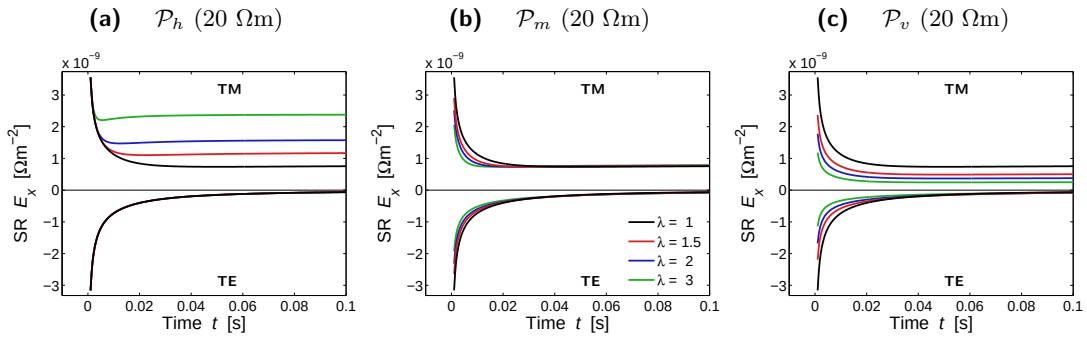

Figure B.1: TE-mode and TM-mode decomposition for step responses in Figure 3.1. A uniform VTI half-space for (a) $\mathcal{P}_h$, (b) $\mathcal{P}_m$, and (c) $\mathcal{P}_v$. The TE-mode is only dependent on the horizontal resistivity, whereas the influence for the TM mode changes gradually from horizontal to mean resistivity with time.

C

Expanded abstract

EAGE Conference & Exhibition 2009, Amsterdam

The research progress was presented by Bruce Hobbs at the Australian Society of Exploration Geophysicists ASEG Conference and Exhibition 2009 in Adelaide, the Canadian Society of Exploration Geophysicists CSEG Convention 2009 in Calgary and the European Association of Geoscientists & Engineers EAGE Conference & Exhibition 2009 in Amsterdam. Folke Engelmark presented at the Indonesian Petroleum Association IPA Convention & Exhibition 2009 in Jakarta and at the Petroleum Geology Conference & Exhibition PGCE 2009 in Kuala Lumpur. An extended abstract is submitted and accepted for a presentation at the Society of Exploration Geophysicists SEG International Exposition 2009 in Houston, which will be given by Bruce Hobbs. Hobbs et al. (2009) is appended here as an example.

Amsterdam '09

P071

The Effect of Resistivity Anisotropy on Transient Electromagnetic Earth Responses

B.A. Hobbs* (PGS), D. Werthmüller (PGS) & F. Engelmark (PGS)

SUMMARY

Resistivity anisotropy is shown to have a dominant effect on earth electromagnetic responses. In particular we consider transverse anisotropy with a vertical axis of symmetry and show the effects of varying anisotropy on land and marine earth step and impulse responses. A single anisotropic response may be inverted with isotropic code resulting in an earth model that satisfies the data but that may be misleading. However an isotropic model cannot be found that fits multi-offset responses from an anisotropic model simultaneously. Thus there is a need to include anisotropy in inversion, either as a fixed or free parameter, and we develop some useful formulae for estimating start values in an inversion scheme.

Introduction

Resistivity anisotropy arises through a variety of scales from micro (e.g. grain size, pore water connectivity) to macro (e.g. laminated sand-shale sequences). For general anisotropy the physical property under consideration may vary in all three spatial directions. The simplest problems involve transverse anisotropy where resistivity at a point in any direction in a plane differs from the value perpendicular to the plane. We are here concerned solely with transverse anisotropy with a vertical axis of symmetry (TIV) so that resistivity at a point has a constant magnitude in any horizontal direction. Induction logs, laterolog and LWD (logging-while-drilling), at least in vertical wells, may be used to examine TIV in particular and these well log results often differ from indirect determinations of resistivity through DC resistivity and general EM surveying. Much of the earlier EM literature considered resistivity as isotropic but there is now great emphasis on the inclusion of anisotropy in modeling and inversion studies. In this paper we consider the effects of transverse anisotropy (specifically TIV) on the earth's electromagnetic impulse and step responses.

The Multi-Transient Electromagnetic Method

In the multi-transient electromagnetic method (Ziolkowski et.al, 2007) current is injected into the ground between two electrodes (the source) and the resulting potential difference is measured between two further electrodes (the receiver). The four electrodes are collinear and the distance between the mid-point of the source electrodes and the mid-point of the receiver electrodes is termed the offset. Transient current injection at the source may take the form of a step change in current, such as a reversal in polarity of a DC current, or a coded, finite-length sequence such as a pseudo-random binary sequence (PRBS). For any form of transient current injection, measurements are made of both the source current and the receiver voltage and deconvolution determines the earth's impulse response. Integration of the impulse response yields the earth's step response.

Earth Step and Impulse Responses

The form of earth response functions may be illustrated by calculating the impulse and step responses at some offset for the simplest case of a uniform, isotropic halfspace. An example step response for land is shown in Figure 1(a) for an offset of 1500 m and a halfspace resistivity of 30 Ω m. Figure 1(b) shows the corresponding impulse response normalized by its peak value of 5.49 10^{-8} $\Omega m^{-2}s^{-1}$. Figure 1(c) shows a marine impulse response calculated at an offset of 1500 m for a uniform halfspace of 1 Ωm overlain by 100 m of sea water of resistivity 0.3125 Ωm. The earth impulse response has been normalized by its peak value of 1.40 10^{-10} $\Omega m^{-2}s^{-1}$. Note the different timescales for land and marine.

On land the impulse response comprises a so-called airwave (which travels along the ground/air interface at a scale comparable to the velocity of light and so arrives at time t=0) followed by a response resulting from diffusion through the resistive subsurface. These two components are immediately separable. In the marine case the earth response comprises travel through the sea water, through the sea/air interface and through the subsurface. All three parts persist throughout the entire record. The peak value and arrival time of the peak value (Tpeak) depend on the subsurface resistivity.

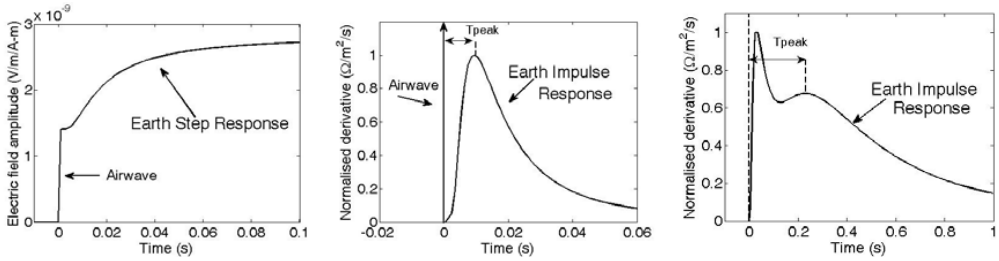

Figure 1. (a) Land step response (b) land impulse response (c) marine impulse response.

The effects of anisotropy

For the transverse anisotropy under consideration (TIV) the vertical resistivity ρ_v and the horizontal resistivity ρ_h define the anisotropy factor

$$\lambda = \sqrt{\frac{\rho_v}{\rho_h}}$$

with typical values between 1 and 5. The square of the geometric mean resistivity is $\rho^2 = \rho_v \rho_h$. We may now consider three special ways of varying anisotropy – keeping ρ_v, ρ_h or ρ^2 constant. We describe these cases as:

ρ_h^c: ρ_h =constant, ρ_v and ρ^2 increase with increasing λ

ρ_v^c: ρ_v =constant, ρ_h and ρ^2 decrease with increasing λ

ρ_c^2: ρ^2 = constant, ρ_h decreases and ρ_v increases with increasing λ

Effects on a uniform halfspace step response for these three cases of varying anisotropy are shown in Figure 2. The effects are dramatic. The airwave (initial step $E(0)$) depends only on the horizontal resistivity ρ_h (since the airwave is the Transverse Electric (TE) mode) whereas the late time DC value ($E(\infty)$) depends only on the geometric mean. Using results from Wilson (1997) for an isotropic halfspace of resistivity ρ

$$E(0) = \frac{\rho}{2\pi r^3} \text{ and hence} = \frac{\rho_h}{2\pi r^3} \quad , \qquad E(\infty) = \frac{\rho}{\pi r^3} \text{ and hence } = \frac{\sqrt{\rho_v \rho_h}}{\pi r^3}.$$

This provides a method of determining the anisotropy of the halfspace as

$$\lambda = \frac{\sqrt{\rho_v \rho_h}}{\rho_h} = \frac{1}{2}\frac{E(\infty)}{E(0)}$$

and this value could be used as an initial start value in an inversion scheme.

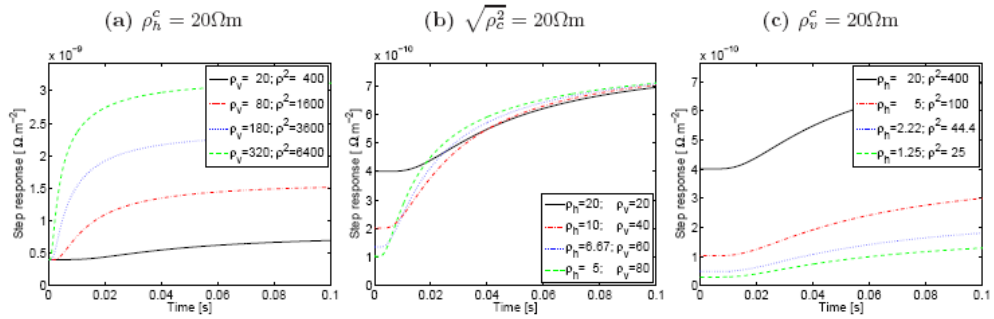

Figure 2. Effects of anisotropy on step responses at an offset of 2 km for a uniform halfspace. λ =1 (solid black), λ =2 (dash-dotted red), λ =3 (dotted blue) and λ =4 (dashed green). The isotropic case (solid black) is the same in all three cases.

Effects on the impulse response for the same models as above are shown in Figure 3. These graphs are the derivatives of those in Figure 2 but the airwave delta function (derivative of the initial step) is not shown.

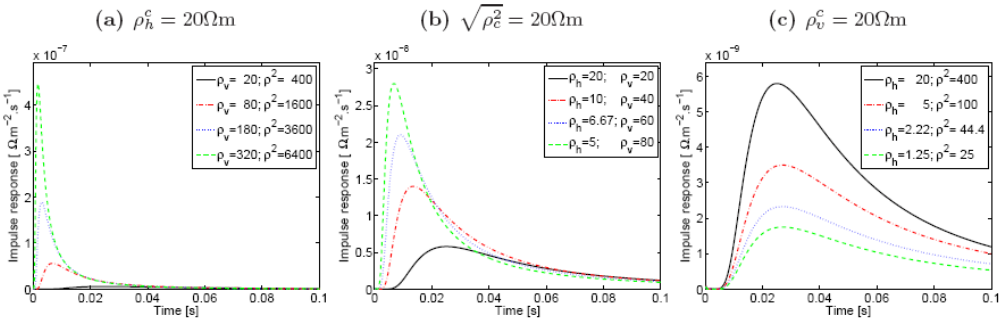

Figure 3. Effects of anisotropy on impulse responses at an offset of 2 km for a uniform halfspace (land case). λ =1 (solid black), 2 (dash-dotted red), 3 (dotted blue) and 4 (dashed green). The isotropic case (solid black) is the same in all three cases.

Marine impulse responses are also much affected by anisotropy as shown in Figure 4. The airwave part is seen to depend mainly on ρ_h and the earth response (overlapping with the airwave) is more dependent on ρ_v.

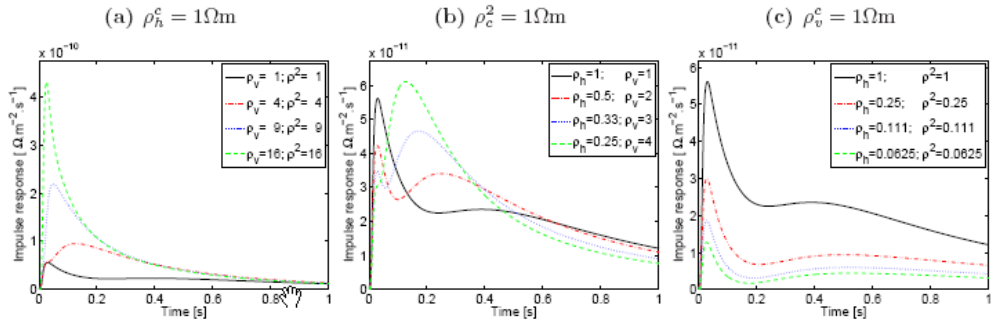

Figure 4. Effects of anisotropy on impulse responses at an offset of 2 km for a uniform halfspace (marine case, water depth = 100 m). λ =1 (solid black), 2 (dash-dotted red), 3 (dotted blue) and 4 (dashed green). The isotropic case (solid black) is the same in all three cases.

Implications for the inversion of Multi-Transient EM data

We now seek to determine the implications of inverting Multi-Transient EM data acquired over an anisotropic subsurface with an isotropic inversion routine. Anisotropic data were generated from a model comprising a background geometric mean resistivity of 20 Ωm with an embedded target layer 25 m thick with geometric mean resistivity 500 Ωm whose top was at a depth of 500 m. An anisotropy value λ =2 was used for all layers. Step responses were generated for the three offsets 1.5 km, 2 km and 2.5 km. Isotropic inversions were made for these three offsets individually (single-trace inversion) and for all three simultaneously (multi-trace inversion) see Figure 5.

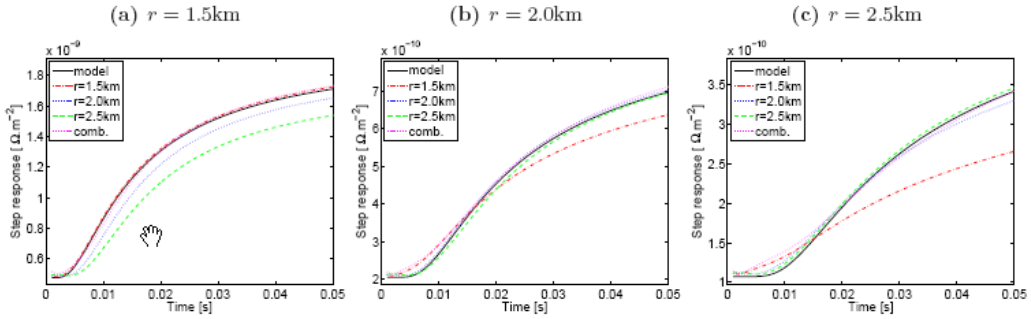

Figure 5. Synthetic step responses from the model described in the text (solid black) and isotropic inversions for three offsets singly and in combination. Also shown are responses at each offset from all the inversion models.

Figure 5 shows that for any single offset an isotropic model can be found that fits the anisotropic response data. The target in these isotropic inversion models is always shallower than in the original anisotropic model – the smaller the offset, the shallower the target. (A survey over a calibration well could be used to determine anisotropy values that yield the correct target depths.) The model derived from inverting the response at one offset was used to calculate the response at other offsets and there are clear misfits (Figure 5). Similarly the use of all three offsets in a multi-trace isotropic inversion failed to produce a model satisfying all the anisotropic data.

Conclusions

Inversion at a single offset cannot distinguish between isotropy and anisotropy and can give misleading results concerning target depths. Thus proper interpretation will require anisotropy to be included as part of any inversion scheme. Since single offset data cannot determine anisotropy, simultaneous inversion of multi-offset data will be a necessity. Layer anisotropies will therefore be included as free parameters in forthcoming inversions. Where possible, a survey over a calibration well may be used to determine anisotropy values that yield the correct target depths.

References

Ziolkowski,A.M., Hobbs,B.A. and Wright,D.A. [2007] Multitransient electromagnetic demonstration survey in France. Geophysics 72 (4), F197-F209.
Wilson,A.J.S. [1997] The equivalent wavefield concept in multichannel transient electromagnetic surveying. Ph.D Thesis, University of Edinburgh.

Acknowledgements

We thank both Nigel Edwards and the Consortium for Electromagnetic Modelling and Inversion (CEMI) for the use of their forward modelling codes incorporating resistivity anisotropy.

D

Codes

MTEM1D_INV and ZOHDY_ANISO

The current release of the isotropic inversion code `MTEM1D_INV` (version `2_2_0`, written in Fortran 90) was extended for VTI. It can now handle conventional isotropic inversions, inversions with fixed anisotropy coefficients and anisotropic inversions, as illustrated in Chapter 6.

The Matlab-code `ZOHDY_ANISO` uses apparent resistivities and apparent anisotropies to invert for a $1\mathcal{D}$ resistivity model, as shown in Chapter 5.

This Chapter acts as an annex to the user guide for `MTEM1D_INV`, and as a brief user guide for `ZOHDY_ANISO`.

D.1 MTEM1D_INV

The anisotropy working directory is a branch of the http://pgsportal/bu/dpt/ge/em/procinv/SharedDocuments/User%20Guides trunk at version `2_2_0` (revision nr. 13015), but all changes to the isotropic code were updated to revision nr. 14127.

The source code can be found on the internal repository, https://edifs20/repo/Projects/Inversion/MTEM1D_INV/Branches/Anisotropy.

Additions to the user guide

The user guide for the isotropic code `MTEM1D_INV` is available on the PGS share point. The explanations here are meant to serve as additional information to this user guide. The numbers here relate to the existing user guide.

6.1.34 Line 34, Anisotropy type
This switch defines whether the inversion is run for the isotropic, fixed anisotropic or free anisotropic case.

- **6.1.34.1 Case (1) Isotropic inversion**
  The inversion behaves like the isotropic `MTEM1D_INV` inversion (it inverts therefore for ρ with $\lambda = 1$ for every layer).
- **6.1.34.2 Case (2) Free anisotropic inversion**
  Free inversion for ρ_h and ρ_v for every layer. This means that the number of unknowns equals twice the number of layers. More data points than the number of unknowns must be provided.
- **6.1.34.3 Case (3) Fixed anisotropic inversion**
  The inversion behaves like the isotropic `MTEM1D_INV` inversion, but with values for λ which have to be defined for every layer (it inverts in fact for ρ_m). The anisotropies must be provided in a file `anisotropy.dat` which contains on every line the anisotropy value for this layer. The number of lines should correspond to the number of layers in the model **(Line 58)**.

6.1.36 Line 36, Inversion Type

- **Cases 1 - 14 are adapted for anisotropy**
  Mu search; Fixed Mu; N Free layer; Fixed parameters; Full model inversion; Ridge regression; Multiple offset no airwave, MONA; Normalised MONA; L1 norm reweighted; L2 norm reweighted; MGS reweighted.
- **Cases 15 - 20 are NOT adapted for anisotropy**
  Conjugate gradient L1 norm; Conjugate gradient L2 norm; Conjugate gradient MGS; BEGS, no resistivity variation; BEGS, resistivity variation 10 %; BEGS, resistivity variation 20 %.

6.1.39 Line 39, fixed parameter filename

This ASCII file must contain in addition to the two standard first columns a third column providing layer anisotropy coefficients. The second column represents the horizontal resistivities.

6.1.44 Line 44, Name of start model file (if L43 = 2)

This ASCII file must contain a second column providing layer anisotropy coefficients. The first column represents horizontal resistivities.

7. Output All output files which provide resistivity values contain one additional column for every resistivity column. The provided resistivities are horizontal resistivities ρ_h, and the additional column provides corresponding anisotropy coefficients λ. The corresponding anisotropy columns are appended after all the resistivity columns, if more than one resistivity column is provided (e.g., initial resistivities, final resistivities, initial anisotropies, final anisotropies).

D.2 ZOHDY_ANISO

The Matlab-routine `ZOHDY_ANISO` derives a $1\mathcal{D}$ resistivity model from step and impulse responses. The input is a synthetic resistivity model. The routine then calculates the step and impulse responses for this resistivity model for multiple offsets, and then seeks to match the apparent resistivity and apparent anisotropy curves, as shown in Chapter 5. The code `ZOHDY_ANISO` can be downloaded from the repository, https://edifs20/repo/Projects/Inversion/ANISO/Inversion. The executable `EX1DV1.2_noreturn.exe` must be copied from this directory to the same place as `ZOHDY_ANISO`.

Input parameters

The code is called with the command `ZOHDY_ANISO(inp)`, where `inp` is a structure containing the following elements (anisotropic model showed in Section 5.2 is appended as an example in bold):

inp.th vector containing model thicknesses; **[500 25]**

inp.rh vector containing model horizontal resistivities; **[10 250 10]**

inp.an vector containing model anisotropies; **[2 2 2]**

inp.name model name; **'Anisotropic_Zohdy_1'**

inp.crit convergence criteria: max. number of iterations; flattens-out; desired rms; **[50 0.02 0.1]**

inp.off offsets used; **(1000:500:8000)**

inp.noise 1: no noise, 2: noise; **1**

inp.per percentage of noise; **0.02**

inp.ly number of final layers; **15**

Output files

inp.name_iso.dat 3 columns: depths; horizontal resistivities, anisotropies
The resulting model after the standard, isotropic Zohdy ($\lambda = 1 \Rightarrow \rho_h = \rho$).

inp.name_aniso.dat 3 columns: depths; horizontal resistivities, anisotropies
The resulting model after the expanded, anisotropic Zohdy.

inp.name_relayered.dat 3 columns: depths; horizontal resistivities, anisotropies
The final model after relayering the expanded Zohdy.

inp.name_rms.dat misfit values, and reasons for stopping.

References

Bhattacharya, B. B., and M. K. Sen, 1981, Depth of investigation of collinear electrode arrays over homogeneous anisotropic half-space in direct current methods: Geophysics, **46**, 768–780.

Bhattacharya, R. K., and H. P. Patra, 1968, Direct Current Electric Sounding: Elsevier Publishing Company, volume **9** *of* Methods in Geochemistry and Geophysics.

Cheesman, S. J., R. N. Edwards, and A. D. Chave, 1987, On the theory of sea-floor conductivity mapping using transient electromagnetic systems: Geophysics, **52**, 204–217.

Constable, S. C., R. L. Parker, and C. G. Constable, 1987, Occam's inversion - A practical algorithm for generating smooth models from electromagnetic sounding data: Geophysics, **52**, 289–300.

Edwards, L. S., 1977, A modified pseudosection for resistivity and IP: Geophysics, **42**, 1020–1036.

Edwards, R. N., 2005, Marine controlled source electromagnetics: principles, methodologies, future commercial applications: Surveys in Geophysics, **26**, 675–700.

Edwards, R. N., D. C. Nobes, and E. Gómez-Treviño, 1984, Offshore electrical exploration of sedimentary basins: The effects of anisotropy in horizontally isotropic, layered media: Geophysics, **49**, 566–576.

Evjen, H. M., 1938, Depth factors and resolving power of electrical measurements: Geophysics, **03**, 78–95.

Greenhalgh, S. A., B. Zhou, M. Greenhalgh, L. Marescot, and T. Wiese, 2009, Explicit expressions for the Fréchet derivatives in 3D anisotropic resistivity inversion: Geophysics, **74**, F31–F43.

Hobbs, B. A., and C. C. Dumitrescu, 1997, One-dimensional magnetotelluric inversion using an adaptation of Zohdy's resistivity method: Geophysical Prospecting, **45**, 1027–1044.

Hobbs, B. A., D. Werthmüller, and F. Engelmark, 2009, The effect of resistivity anisotropy on transient electromagnetic earth responses: 71th Meeting, EAGE, P071.

Jing, C., K. Green, and D. Willen, 2008, CSEM inversion: Impact of anisotropy, data coverage, and initial models: 78th Meeting, SEG, 604–608.

Loke, M. H., and R. D. Barker, 1995, Improvements to the Zohdy method for the inversion of resistivity sounding and pseudosection data: Computers & Geosciences, **21**, 321–332.

Long, A., 2007, Mulit-Transient EM Technology at PGS: Technical Report 4, PGS Petroleum Geo-Services, http://www.pgs.com/techlink.

Løseth, L. O., and B. Ursin, 2007, Electromagnetic fields in planarly layered anisotropic media: Geophysical Journal International, **170**, 44–80.

Lu, X., and C. Xia, 2007, Understanding anisotropy in marine CSEM data: 77th Meeting, SEG, 633–637.

Maillet, R., 1947, The fundamental equations of electrical prospecting: Geophysics, **12**, 529–556.

Negi, J. G., and P. D. Saraf, 1989, Anisotropy in Geoelectromagnetism: Elsevier Publishing Company, volume **28** *of* Methods in Geochemistry and Geophysics.

Nordskag, J. I., L. Amundsen, B. Ursin, and L. O. Løseth, 2007, TE and TM Decomposition. Marine EM Surveying by Use of Gradiometers: 59th Meeting, EAGE, Session: P235.

Ramananjaona, C. J., D. L. Andréis, and L. M. MacGregor, 2008, Characterisation of anisotropic resistivity from marine CSEM data: 70th Meeting, EAGE, G002.

Weidelt, P., 2007, Guided waves in marine CSEM: Geophysical Journal International, **171**, 153–176.

Weir, G. J., 1980, Transient electromagnetic fields about an infinitesimally long grounded horizontal electric dipole on the surface of a uniform half-space: Geophysical Journal of the Royal Astronomical Society, **61**, 41–56.

Wilson, A. J. S., 1997, The equivalent wavefield concept in multichannel transient electromag-

netic surveying: Ph.D., University Of Edinburgh.

Wright, D. A., 2003, Detection of hydrocarbons and their movement in a reservoir using time-lapse multi-transient electromagnetic MTEM data: Ph.D., University Of Edinburgh.

Zhdanov, M. S., 2002, Geophysical inverse theory and regularization problems: Elsevier Publishing Company, volume **36** *of* Methods in Geochemistry and Geophysics.

Ziolkowski, A., B. A. Hobbs, and D. A. Wright, 2007, Multitransient electromagnetic demonstration survey in France: Geophysics, **72**, no. 4, F197–F209.

Ziolkowski, A., and D. Wright, 2007, Removal of the airwave in shallow-marine transient EM data: 77th Meeting, SEG, 534–538.

Zohdy, A. A. R., 1989, A new method for the automatic interpretation of Schlumberger and Wenner sounding curves: Geophysics, **54**, 245–253.